

## GEOPHYSICS®

**Adaptive multinary inversion of gravity and gravity  
gradiometry data**

Journal:	<i>Geophysics</i>
Manuscript ID	GEO-2016-0451.R3
Manuscript Type:	Technical Paper
Date Submitted by the Author:	27-Jun-2017
Complete List of Authors:	Zhdanov, Michael; University of Utah, Geology and Geophysics Lin, Wei; University of Utah, Geology and Geophysics
Keywords:	3D, gravity, inversion
Area of Expertise:	Gravity Exploration Methods

SCHOLARONE™  
Manuscripts

# Adaptive multinary inversion of gravity and gravity gradiometry data

Michael S. Zhdanov<sup>123</sup> and Wei Lin<sup>1</sup>

<sup>1</sup>*Consortium for Electromagnetic Modeling and Inversion (CEMI),*

*University of Utah, Salt Lake City, Utah, USA*

<sup>2</sup>*TechnoImaging, Salt Lake City, Utah, USA*

<sup>3</sup>*Moscow Institute of Physics and Technology, Moscow, Russia*

(July 10, 2017)

Running head: **Adaptive multinary inversion of gravity data**

## ABSTRACT

This paper develops a novel approach to inversion of gravity and gravity gradiometry data based on multinary transformation of the model parameters. This concept is a generalization of binary density inversion to the models described by any number of discrete model parameters. The multinary inversion makes it possible to explicitly exploit the sharp contrasts of the density between the host media and anomalous targets in the inversion of gravity and gravity gradiometry data. In the framework of the multinary inversion method, we use the given values of density and error functions to transform the density distribution into the desired step-function distribution. In order to accommodate to a possible deviation of the densities from the fixed discrete values, we introduce an adaptive technique for selecting the corresponding standard deviations, guided by the inversion process. The novel adaptive multinary inversion algorithm is demonstrated to be effective in determining the shape, location, and the densities of the anomalous targets. We show that this method can

1  
2  
3  
4  
5  
6  
7  
8  
9  
10  
11  
12  
13  
14  
15  
16  
17  
18  
19  
20  
21  
22  
23  
24  
25  
26  
27  
28  
29  
30  
31  
32  
33  
34  
35  
36  
37  
38  
39  
40  
41  
42  
43  
44  
45  
46  
47  
48  
49  
50  
51  
52  
53  
54  
55  
56  
57  
58  
59  
60

1  
2  
3  
4 be effectively applied to the inversion of the full tensor gravity gradiometry (FTG) data  
5  
6 computer-simulated for the SEG salt density model and for the field FTG data collected in  
7  
8 Nordkapp Basin, Barents Sea.  
9  
10

1  
2  
3  
4  
5  
6  
7  
8  
9  
10  
11  
12  
13  
14  
15  
16  
17  
18  
19  
20  
21  
22  
23  
24  
25  
26  
27  
28  
29  
30  
31  
32  
33  
34  
35  
36  
37  
38  
39  
40  
41  
42  
43  
44  
45  
46  
47  
48  
49  
50  
51  
52  
53  
54  
55  
56  
57  
58  
59  
60

### INTRODUCTION

Traditional methods of gravity inversion characterize the density distribution in the area of interest by a function, which varies continuously within the given bounds. In order to ensure the unique and stable solution of the gravity inverse problem, one can impose additional conditions on the density, such as minimum norm (Tikhonov and Arsenin, 1977), or maximum smoothness (Constable, et al., 1987) constraints. However, the inverse models produced by traditional inversions are still represented by a continuous distribution of the density over the anomalous targets. At the same time, typical geological structures, such as salt dome, hydrocarbon reservoir, and ore deposits, are usually characterized by a sharp boundary separating the target and a host rock.

In recent years, several techniques have been developed to recover anomalous targets with high contrasts between physical properties and sharp boundaries. For example, one can use focusing regularization (Portniaguine and Zhdanov, 1999; Zhdanov, 2002, 2009) to recover model parameters with sharp physical property contrasts. We should mention also the clustering-based inversion methods, which are usually used to impose the constraints on the inversion results (e.g., Paasche and Tronicke, 2007; Lelièvre et al., 2012; Sun and Li, 2015). However, all these methods still produce a continuous distribution of the physical properties, even if the inverse images become more focused and sharp.

One way of generating sharp boundaries in inverse models is based on using discrete values of the model parameters. An example of this approach is provided by the method of binary inversion, where the model parameters can take two possible discrete values only. A binary inversion algorithm was realized using stochastic optimization methods (e.g. Bosch et al., 2001; Krahenbuhl and Li, 2006), or a level set method (e.g., Osher and Sethian, 1988;

1  
2  
3  
4  
5  
6  
7  
8  
9  
10  
11  
12  
13  
14  
15  
16  
17  
18  
19  
20  
21  
22  
23  
24  
25  
26  
27  
28  
29  
30  
31  
32  
33  
34  
35  
36  
37  
38  
39  
40  
41  
42  
43  
44  
45  
46  
47  
48  
49  
50  
51  
52  
53  
54  
55  
56  
57  
58  
59  
60

Santosa, 1996; Dorn and Lesselier, 2006; Li et al., 2016).

In the paper by Zhdanov and Cox (2013), the binary inversion was extended to any number of discrete values of the model parameters by introducing a novel method based on multinary functions, which are defined as those functions accepting a finite number of discrete values. This concept is a generalization of binary density inversion. The fundamentally new idea of this method is related to the transformation of the continuous density distribution into the desired step-function distribution using the given discrete values of density and the error functions. The degree of “sharpness” of the inverse density model is determined by the values of the corresponding standard deviations of the error functions, used for the multinary transform. The small values of the standard deviation generate a focused image of the density model with sharp boundaries, while the large values produce a relatively smooth model. Therefore, selection of the optimal values of the corresponding standard deviation represents a critical element of multinary inversion method. In this paper, we introduce a solution of this problem based on adaptive adjustment of the values of the corresponding standard deviation during the inversion process based on regularized conjugate gradient method. We call this method *an adaptive multinary inversion*.

We have developed an algorithm of adaptive multinary inversion for gravity and gravity gradiometry data. The method was tested on 3D synthetic models and also applied to the gravity data generated for an SEG salt dome density model. We also present a case study for the adaptive multinary inversion of the FTG gravity gradiometry data acquired in Nordkapp Basin of the Barents Sea.

## INVERSE PROBLEM FORMULATION

The gravity inverse problem can be formulated as a solution of the following operator equation:

$$\mathbf{d} = \mathbf{A}(\boldsymbol{\rho}), \quad (1)$$

where  $\mathbf{A}$  is a linear operator for computing the gravity field,  $\mathbf{d}$  are the observed gravity field data, which may include the gravity field,  $G_z$ , and all components of the full gravity gradient tensor, and  $\boldsymbol{\rho}$  represents the model density. In a case of the discrete inverse problem, the density distribution  $\boldsymbol{\rho}$  can be represented as a vector formed by  $N_m$  components:

$$\boldsymbol{\rho} = [\rho_1, \rho_2, \dots, \rho_{N_m}]^T, \quad (2)$$

and the observed data  $\mathbf{d}$  can be considered as an  $N_d$ -dimensional vector,

$$\mathbf{d} = [d_1, d_2, \dots, d_{N_d}]^T, \quad (3)$$

where  $N_m$  is the number of unknown model parameters (e.g., number of the discretization cells in the inverse model);  $N_d$  is the number of the data points; and superscript “ $T$ ” denotes the transposition operation.

Usually, the inverse problem 1 is ill-posed, and we solve this problem using the regularization method by minimizing the corresponding parametric functional:

$$P(\boldsymbol{\rho}) = \|\mathbf{W}_d(\mathbf{A}(\boldsymbol{\rho}) - \mathbf{d})\|^2 + \alpha \|\mathbf{W}_m(\boldsymbol{\rho} - \boldsymbol{\rho}_{apr})\|^2 \longrightarrow \min, \quad (4)$$

where  $\mathbf{W}_d$  and  $\mathbf{W}_m$  are the data and model weighting matrices,  $\boldsymbol{\rho}_{apr}$  is the a priori given density distribution, and  $\alpha$  is a regularization parameter, which provides a balance between the misfit,  $\|\mathbf{W}_d(\mathbf{A}(\boldsymbol{\rho}) - \mathbf{d})\|^2$ , and stabilizing,  $\|\mathbf{W}_m(\boldsymbol{\rho} - \boldsymbol{\rho}_{apr})\|^2$ , functionals. This minimization problem 4 can be solved using the regularized conjugate gradient method (Zhdanov, 2002, 2015). Note that, the model weighting matrix,  $\mathbf{W}_m$ , is selected as a square

root of the integrated sensitivity matrix, which is equivalent to including a depth weighting factor in the inversion algorithm (Zhdanov, 2002).

In a general case, the recovered density distribution is described by a continuous function. In some geophysical applications, the desired physical property (e.g., density in the case of a gravity inverse problem) can be described by the binary function as follows:

$$\bar{m}_i = \left\{ m_i^{(1)} = 0, m_i^{(2)} = 1 \right\}, \quad (5)$$

or by the ternary function:

$$\bar{m}_i = \left\{ m_i^{(1)} = -1, m_i^{(2)} = 0, m_i^{(3)} = 1 \right\}. \quad (6)$$

Further, we can extend the description of the distribution of a physical property (e.g., density) using the multinary function of order  $P$ , having discrete number of values:

$$\bar{m}_i = \left\{ m_i^{(1)}, m_i^{(2)}, \dots, m_i^{(P)} \right\}. \quad (7)$$

The main difficulty with using multinary functions in the regularized gradient type inversion is that the derivative-based minimization of the Tikhonov parametric functional is difficult to implement. In order to overcome this difficulty, Zhdanov and Cox (2013) introduced a transform of the model parameters and their sensitivities from the continuous functions to their multinary function representation using monotonically increasing functions. As a result, one can arrive at the conventional inverse problem, which could be solved using a standard gradient-type method.

## MULTINARY MODEL TRANSFORM

The nonlinear transformation of the continuous function into the multinary function can be described as follows. We transform the original vector of anomalous density distribution,

1  
2  
3  
4  
5  
6  
7  
8  
9  
10  
11  
12  
13  
14  
15  
16  
17  
18  
19  
20  
21  
22  
23  
24  
25  
26  
27  
28  
29  
30  
31  
32  
33  
34  
35  
36  
37  
38  
39  
40  
41  
42  
43  
44  
45  
46  
47  
48  
49  
50  
51  
52  
53  
54  
55  
56  
57  
58  
59  
60

$\boldsymbol{\rho} = [\rho_1, \rho_2, \dots, \rho_{N_m}]^T$ , into a new vector model space,  $\tilde{\boldsymbol{\rho}} = [\tilde{\rho}_1, \tilde{\rho}_2, \dots, \tilde{\rho}_{N_m}]^T$ , defined by a number of discrete (multinary) densities,  $\rho^{(j)}$  ( $j = 1, 2, \dots, P$ ), using a superposition of error functions:

$$\tilde{\rho}_i = E_\sigma(\rho_i) = c\rho_i + \frac{1}{2} \sum_{j=1}^P \left[ 1 + \operatorname{erf} \left( \frac{\rho_i - \rho^{(j)}}{\sqrt{2}\sigma} \right) \right], \quad i = 1, \dots, N_m; \quad (8)$$

where the error function,  $\operatorname{erf}(z)$ , is defined as follows:

$$\operatorname{erf}(z) = \frac{2}{\sqrt{\pi}} \int_0^z e^{-t^2} dt, \quad (9)$$

and parameter  $\sigma$  is a standard deviation of the value  $\rho^{(j)}$ . The important property of function  $E_\sigma(\rho_i)$  is that it is a monotonically increasing function.

We will call  $\tilde{\rho}_i$  the “quasi-multinary densities”, because they are described by some smoothed step functions. We use the quasi-multinary density as an approximation of the strict multinary function in order to avoid the singularities in the inverse multinary transform. The constant  $c$  is a small number to avoid singularities in the calculation of the derivatives of the quasi-multinary densities,  $\tilde{\rho}_i$ , and  $P$  is a total number of discrete (multinary) values of the model parameters (densities),  $\rho^{(j)}$ . The discrete densities,  $\rho^{(j)}$  ( $j = 1, 2, \dots, P$ ), can be chosen a priori based on the known geological information (e.g., core samples). We will show below that it is not necessary to know the discrete densities exactly. The multinary inversion produces a stable result even in a case of some differences between the true (estimated) discrete values of the density model and multinary densities present in formula 8.

Note that, the derivative of the error function 9 is equal to the corresponding Gaussian function, therefore the derivative of the quasi-multinary densities,  $\tilde{\rho}_i$ , can be calculated as

a superposition of the Gaussian functions,  $G_\sigma \left( \rho_i - \rho_i^{(j)} \right)$ , as follows:

$$\frac{\partial \tilde{\rho}_i}{\partial \rho_i} = \frac{\partial E_\sigma(\rho_i)}{\partial \rho_i} = g_\sigma(\rho_i) = \sum_{j=1}^P G_\sigma \left( \rho_i - \rho_i^{(j)} \right) + c, \quad (10)$$

where

$$G_\sigma \left( \rho_i - \rho_i^{(j)} \right) = \frac{1}{\sqrt{2\pi}\sigma_i} \exp \left( -\frac{\left( \rho_i - \rho_i^{(j)} \right)^2}{2\sigma_i^2} \right). \quad (11)$$

One can see that introducing  $c > 0$  ensures that this derivative is always positive,  $\partial E_\sigma(\rho_i)/\partial \rho_i > 0$ , which confirms the monotonic nature of function  $E_\sigma(\rho_i)$ .

Expressions 8 and 10 demonstrate that the quasi-multinary function can be interpreted using an analogy from statistics, where the Gaussian function 11 represents *the probability density function (PDF)* of each discrete density  $\rho_i$  with the mean value  $\rho_i^{(j)}$  and the standard deviation  $\sigma$  (Zhdanov, 2015). The quasi-multinary function,  $E_\sigma(\rho_i)$ , can be treated as a corresponding *cumulative density probability function (CDFP)* of each discrete density,  $\rho_i$ , considered as a random variable.

Panel (a) in Figure 1 presents an example of the quasi-multinary function (*cumulative density probability function*) of three discrete densities, while panel (b) shows its derivative (*probability density function*), where values of the discrete densities are as follows:  $-1.0 \text{ g/cm}^3$ ,  $0.0 \text{ g/cm}^3$ ,  $0.5 \text{ g/cm}^3$ , and  $\sigma = 0.02$ . One can see from this figure how a continuous distribution of the anomalous density along the horizontal axis can be transformed into the step-wise distribution,  $E(\rho_i)$ , along the vertical axis. It is also important to note that, according to the basic principles of statistics, the small values of the standard deviation  $\sigma$  correspond to the narrow Gaussian probability distribution, while the large  $\sigma$  generates wide and smooth probability function. In terms of the quasi-multinary functions this means that these functions provide a more accurate approximation of the strict multinary functions for a smaller standard deviation  $\sigma$ . In other words, the quasi-multinary transform 8 with the

small  $\sigma$  produces a more focused and sharp inverse density model than that with a large standard deviation. Thus, the choice of the optimal values of standard deviations used in the quasi-multinary transform represents one of the critical problems of the inversion.

## INVERSION ALGORITHM

As a result of the multinary model transform, the original density distribution,  $\rho$ , is changed into the transformed distribution,  $\tilde{\rho}$ . Therefore, the original inverse problem 1 takes the following form:

$$\mathbf{d} = \mathbf{A}[E_{\sigma}^{-1}(\tilde{\rho})] = \tilde{\mathbf{A}}_{\sigma}(\tilde{\rho}), \quad (12)$$

where  $\tilde{\mathbf{A}}_{\sigma}$  is the new forward modeling operator acting in the transformed model space  $\tilde{\rho}$ . We should note that, the inverse transform (from transformed distribution,  $\tilde{\rho}$ , back to original density distribution,  $\rho$ ) cannot be described by an analytic function. Therefore, in order to implement numerically the inverse transform, one have to create a densely sampled look-up table over a range of the model parameters. The transformed parameters are then converted back to the original model space with interpolation.

We solve the inverse problem 12 based on the minimization of the following Tikhonov parametric functional:

$$P_{\sigma}(\tilde{\rho}) = \left\| \mathbf{W}_d(\tilde{\mathbf{A}}_{\sigma}(\tilde{\rho}) - \mathbf{d}) \right\|^2 + \alpha_n \left\| \tilde{\mathbf{W}}_m(\tilde{\rho} - \tilde{\rho}_{apr}) \right\|^2 \longrightarrow \min. \quad (13)$$

Remarkably, the original parametric functional 4 is always convex for linear forward operator  $\mathbf{A}$  and has a unique global minimum (Tikhonov and Arsenin, 1977; Zhdanov, 2002). This property of the Tikhonov parametric functional ensures the convexity of the modified functional,  $P_{\sigma}(\tilde{\rho})$ , because transformation  $E_{\sigma}$  into the multinary model space is a known monotonically increasing function.

We apply the regularized conjugate gradient (RCG) method to find the global minimum of the parametric functional  $P_\sigma(\tilde{\rho})$  (Zhdanov, 2002, 2015):

$$\begin{aligned}
 \mathbf{r}_n &= \tilde{\mathbf{A}}_\sigma(\tilde{\rho}_n) - \mathbf{d}, \\
 \mathbf{l}_n^\sigma &= \tilde{\mathbf{F}}_{\sigma,n}^T \mathbf{W}_d^2 \mathbf{r}_n + \alpha_n \mathbf{W}_m^2 (\tilde{\rho}_n - \tilde{\rho}_{apr}), \\
 \beta_n^\sigma &= \|\mathbf{l}_n^\sigma\|^2 / \|\mathbf{l}_{n-1}^\sigma\|^2, \\
 \tilde{\mathbf{l}}_n^\sigma &= \mathbf{l}_n^\sigma + \beta_n^\sigma \tilde{\mathbf{l}}_{n-1}^\sigma, \tilde{\mathbf{l}}_0^\sigma = \mathbf{l}_0^\sigma, \\
 k_n^\sigma &= (\tilde{\mathbf{l}}_n^\sigma, \mathbf{l}_n^\sigma) / \left[ \|\mathbf{W}_d \tilde{\mathbf{F}}_{\sigma,n} \tilde{\mathbf{l}}_n^\sigma\|^2 + \alpha_n \|\mathbf{W}_m \tilde{\mathbf{l}}_n^\sigma\|^2 \right], \\
 \tilde{\rho}_{n+1} &= \tilde{\rho}_n - k_n^\sigma \tilde{\mathbf{l}}_n^\sigma,
 \end{aligned} \tag{14}$$

where  $\tilde{\mathbf{F}}_\sigma$  is the corresponding Fréchet derivative operator for  $\tilde{\mathbf{A}}_\sigma$ .

As one can see, equations 12 through 14 include standard deviation  $\sigma$  as a parameter. For a relatively simple synthetic model, a fixed standard deviation  $\sigma$  usually works well for the multinary inversion. However, in a case of inversion of the field gravity data, a fixed  $\sigma$  cannot guarantee the convergence. Indeed, in a case of small  $\sigma$  we assume that the density distribution in the subsurface could not deviate significantly from a number of preselected fixed discrete values,  $\rho^{(j)}$  ( $j = 1, 2, \dots, P$ ), used in the definition of the multinary transform 8. However, the actual distribution of the densities in the subsurface may be significantly different from the given values of  $\rho^{(j)}$ . In this case we will observe a slow convergence of the RCG algorithm, or even flatter of the results of the inversion, because the model parameters would not have enough freedom to accommodate to the observed gravity data. In order to overcome this problem, one should increase the standard deviation to provide more flexibility for the density distribution of the inverse model to fit the observed data.

We have developed a method of adaptive multinary inversion, which implements the approach outlined above by automatically increasing the standard deviation during the

1  
2  
3  
4  
5  
6  
7  
8  
9  
10  
11  
12  
13  
14  
15  
16  
17  
18  
19  
20  
21  
22  
23  
24  
25  
26  
27  
28  
29  
30  
31  
32  
33  
34  
35  
36  
37  
38  
39  
40  
41  
42  
43  
44  
45  
46  
47  
48  
49  
50  
51  
52  
53  
54  
55  
56  
57  
58  
59  
60

RCG iterative process if the misfit does not decrease fast enough. In the framework of this approach, the standard deviation,  $\sigma_n$ , for each iteration,  $n$ , is determined according to the following formula:

$$\sigma_n = \begin{cases} \sigma_{n-1} + \delta\sigma, & \text{if } \nabla\varphi_n < \nabla\varphi_{n-1}, \\ \sigma_{n-1}, & \text{if } \nabla\varphi_n \geq \nabla\varphi_{n-1}, \\ \sigma_{\max}, & \text{if } \sigma_n > \sigma_{\max}, \end{cases} \quad (15)$$

where  $\delta\sigma$  is the increment of the adaptive standard deviation,  $\sigma_n$ ;  $\nabla\varphi_n$  is the gradient of the normalized misfit,

$$\nabla\varphi_n = \left\{ \left\| \mathbf{W}_d(\tilde{\mathbf{A}}_{\sigma_n}(\tilde{\boldsymbol{\rho}}) - \mathbf{d}) \right\|^2 - \left\| \mathbf{W}_d(\tilde{\mathbf{A}}_{\sigma_{n-1}}(\tilde{\boldsymbol{\rho}}) - \mathbf{d}) \right\|^2 \right\} / \left\| \mathbf{W}_d \mathbf{d} \right\|^2; \quad (16)$$

and  $\sigma_{\max}$  is the given upper limit of  $\sigma$  to ensure the validity of the multinary approach.

In order to calculate the Fréchet derivative with respect to the new model parameters,  $\tilde{\boldsymbol{\rho}}$ , we apply the variational operator  $\delta_{\tilde{\boldsymbol{\rho}}}$  to equation 12, as follows:

$$\delta_{\tilde{\boldsymbol{\rho}}} \mathbf{d} = \delta_{\tilde{\boldsymbol{\rho}}} \mathbf{A}[E_{\sigma}^{-1}(\tilde{\boldsymbol{\rho}})] = \mathbf{A} \delta_{\tilde{\boldsymbol{\rho}}} \boldsymbol{\rho}. \quad (17)$$

We note that, according to equation 10, variation  $\delta_{\tilde{\boldsymbol{\rho}}} \boldsymbol{\rho}$  can be calculated using scalar notations as follows:

$$\delta_{\tilde{\rho}_i} \rho_i = g_{\sigma}^{-1}(\rho_i) \delta \tilde{\rho}_i. \quad (18)$$

Formula 18 in matrix notations has the following form:

$$\delta_{\tilde{\boldsymbol{\rho}}} \boldsymbol{\rho} = \mathbf{g}_{\sigma}^{-1}(\boldsymbol{\rho}) \delta \tilde{\boldsymbol{\rho}}, \quad (19)$$

where  $\mathbf{g}_{\sigma}$  is a diagonal matrix formed by the scalar components  $g_{\sigma}(\rho_i)$ ,  $i = 1, 2, \dots, N_m$ .

Substituting 19 into 17, we find

$$\delta_{\tilde{\boldsymbol{\rho}}} \mathbf{d} = \mathbf{A} \mathbf{g}_{\sigma}^{-1}(\boldsymbol{\rho}) \delta \tilde{\boldsymbol{\rho}} = \tilde{\mathbf{F}}_{\sigma} \delta \tilde{\boldsymbol{\rho}}. \quad (20)$$

Thus, the Fréchet derivative  $\tilde{\mathbf{F}}_\sigma$  with respect to the new model parameter,  $\tilde{\rho}$ , can be derived as follows:

$$\tilde{\mathbf{F}}_\sigma = \mathbf{A}\mathbf{g}_\sigma^{-1}. \quad (21)$$

In summary, the algorithm of adaptive multinary inversion can be described by the following iterative process:

$$\begin{aligned} \mathbf{r}_n &= \tilde{\mathbf{A}}_{\sigma_n}(\tilde{\rho}_n) - \mathbf{d}, \\ \mathbf{l}_n^{\sigma_n} &= \mathbf{g}_{\sigma_n}^{-1}\mathbf{A}^T\mathbf{W}_d^2\mathbf{r}_n + \alpha_n\tilde{\mathbf{W}}_m^2(\tilde{\rho}_n - \tilde{\rho}_{apr}), \\ \beta_n^{\sigma_n} &= \|\mathbf{l}_n^{\sigma_n}\|^2 / \|\mathbf{l}_{n-1}^{\sigma_n}\|^2, \\ \tilde{\mathbf{l}}_n^{\sigma_n} &= \mathbf{l}_n^{\sigma_n} + \beta_n^{\sigma_n}\tilde{\mathbf{l}}_{n-1}^{\sigma_n}, \tilde{\mathbf{l}}_0^{\sigma_n} = \mathbf{l}_0^{\sigma_n}, \\ k_n^{\sigma_n} &= (\tilde{\mathbf{l}}_n^{\sigma_n}, \mathbf{l}_n^\alpha) / \left[ \|\mathbf{W}_d\mathbf{A}\mathbf{g}_{\sigma_n}^{-1}\tilde{\mathbf{l}}_n^{\sigma_n}\|^2 + \alpha_n\|\tilde{\mathbf{W}}_m\tilde{\mathbf{l}}_n^{\sigma_n}\|^2 \right], \\ \tilde{\rho}_{n+1} &= \tilde{\rho}_n - k_n^{\sigma_n}\tilde{\mathbf{l}}_n^{\sigma_n}, \end{aligned} \quad (22)$$

where the standard deviation,  $\sigma_n$ , is updated according to formula (15). The regularization parameter  $\alpha_n$  is usually selected as  $\alpha_n = \alpha_0 \cdot q^{n-1}$ , where constant  $q$  is a small number,  $0 < q < 1$ . In the following synthetic model studies,  $q$  was set at 0.9.

This concludes a description of the method of the adaptive multinary inversion.

## SYNTHETIC MODEL STUDY

### *Synthetic Model 1: Two-body model*

In this section, we test the developed algorithm of multinary inversion using a 3D synthetic model with two bodies with different sizes, densities and burial depths: the small body with negative anomalous density of  $-1 \text{ g/cm}^3$  has a size of  $400 \text{ m} \times 400 \text{ m} \times 400 \text{ m}$ , and its center is located at a depth of 400 m; the relatively large body with positive anomalous

1  
2  
3  
4  
5  
6  
7  
8  
9  
10  
11  
12  
13  
14  
15  
16  
17  
18  
19  
20  
21  
22  
23  
24  
25  
26  
27  
28  
29  
30  
31  
32  
33  
34  
35  
36  
37  
38  
39  
40  
41  
42  
43  
44  
45  
46  
47  
48  
49  
50  
51  
52  
53  
54  
55  
56  
57  
58  
59  
60

density of  $0.5 \text{ g/cm}^3$  has a size of  $800 \text{ m} \times 800 \text{ m} \times 800 \text{ m}$  and its center is located at a depth of 1000 m. The horizontal distance between two bodies is of 3600 m. The value of the background density was set at 0. The synthetic gravity field  $G_z$ , contaminated by 3% Gaussian noise, was used as the observed data. The 3% is the peak noise level of the synthetic observed data, where the mean value and the standard deviation are 1.5% and 0.5%, respectively. The multinary function was set to recover three discrete densities of  $0 \text{ g/cm}^3$ ,  $-1 \text{ g/cm}^3$  and  $0.5 \text{ g/cm}^3$  (where value 0 represents the background density model) with fixed standard deviation  $\sigma = 0.02$ . The representation of the multinary model transform and its derivative are shown in Figure 1 panel (a) and (b). The iterative process of the RCG algorithm was terminated when the norm of the difference between the observed and predicted data reached the level of noise, 3%.

Figure 2, panel (a), presents the profiles of the predicted gravity field (solid line) and the synthetic gravity field  $G_z$  (dotted line), obtained by the inversion, at  $Y = 3500 \text{ m}$  (Northing). Panel (b) in the same Figure shows the vertical cross section of the synthetic model, corresponding to this profile, while panels (c), (d) and (e) provide the same cross sections of the recovered density distribution using conventional, focusing, and multinary inversions, respectively. In the case of conventional inversion, we assumed that the density distribution was represented by a continuous function, and we applied a standard regularized conjugate gradient method with the minimum norm stabilizer (Zhdanov, 2002). In the case of focusing inversion, we applied a reweighted regularized conjugate gradient method with the minimum support stabilizer (Portniaguine and Zhdanov, 1999; Zhdanov, 2002). One can see that the conventional inversion with the minimum norm stabilizer failed to recover the correct values of the densities and locations of the anomalous bodies. The focusing inversion produced a more contrast plot with the clearer images of the bodies; however,

1  
2  
3  
4  
5  
6  
7  
8  
9  
10  
11  
12  
13  
14  
15  
16  
17  
18  
19  
20  
21  
22  
23  
24  
25  
26  
27  
28  
29  
30  
31  
32  
33  
34  
35  
36  
37  
38  
39  
40  
41  
42  
43  
44  
45  
46  
47  
48  
49  
50  
51  
52  
53  
54  
55  
56  
57  
58  
59  
60

these images were still diffused and the density values were underestimated. Finally, the multinary inversion successfully recovered the target bodies with sharp boundaries and correct values of the densities. Figure 3 presents a 3D view of the true Model 1 (panel a), and the multinary inversion result (panel b). Thus, the multinary inversion is able to image both the shallow and deep bodies at their approximate locations and densities. Actually, the top of the bodies was determined quite well, while the depth to the bottom was underestimated, which was a typical result for gravity inversion.

The above inversion results were based on the multinary function with the same densities as for the synthetic models. What happens if we choose the wrong densities? In order to investigate this situation, we introduce the multinary function with three discrete densities of  $0 \text{ g/cm}^3$ ,  $-0.7 \text{ g/cm}^3$  and  $0.35 \text{ g/cm}^3$ , which are different from the true model. Figure 4 shows the representations of the multinary model transform and its derivative with the wrong densities (dotted line) and with the true densities (solid line). Figure 5 (a) and (b) show the data fitting using the right and wrong densities. Figure 5 (c) provides the same cross sections of the recovered density distribution as Figure 2 (d) using the multinary inversion with the true densities, while panel (d) shows the same cross sections of the multinary inversion result with the wrong densities. We can see that the recovered sizes of the two anomalous bodies produced using the wrong densities are slightly larger than those for the previous inversion results with the correct densities. However, overall, the new inverse model still represent the true model reasonably well.

#### *Synthetic Model 2: Modified SEG salt density model*

In this section we will use the SEG salt model to test the multinary inversion. Figure 6 represents a 3D view of this model. We have simplified this model slightly by considering

1  
2  
3  
4  
5  
6  
7  
8  
9  
10  
11  
12  
13  
14  
15  
16  
17  
18  
19  
20  
21  
22  
23  
24  
25  
26  
27  
28  
29  
30  
31  
32  
33  
34  
35  
36  
37  
38  
39  
40  
41  
42  
43  
44  
45  
46  
47  
48  
49  
50  
51  
52  
53  
54  
55  
56  
57  
58  
59  
60

the anomalous targets associated with the salt dome only. The density of the salt dome was set as  $-0.5 \text{ g/cm}^3$ , and the value of background density was 0.

The synthetic full tensor gravity gradiometry (FTG) data, contaminated by 1% Gaussian noise, were used as the observed data. The 1% is the peak noise level of the synthetic observed data, where the mean value and the standard deviation are 0.5% and 0.17%, respectively. In this synthetic model study the multinary inversion was set to recover two discrete densities of  $0 \text{ g/cm}^3$  and  $-0.5 \text{ g/cm}^3$  with fixed standard deviation  $\sigma = 0.05$ . The representation of the multinary model transform and its derivative are shown in Figure 7 panels (a) and (b). The iterative process of the RCG algorithm was terminated when the norm of the difference between the observed and predicted data reached the level of noise, 1%.

Figure 8 shows the synthetic gravity field of the SEG salt model, while the two white lines indicate the location of profiles A ( $Y = 1900 \text{ m}$ ) and B ( $Y = 2600 \text{ m}$ ). For the gravity data inversion, the vertical cross sections of the synthetic model are given in Figure 9, panels (a2) and (b2), while panels (a3)-(b3) and (a4)-(b4) show the cross sections of the recovered models using the conventional smooth and multinary inversions, respectively. One can see that, the conventional inversion can only show a weak anomaly near the surface; however, the multinary inversion determines the approximate location of the salt dome and its true density. For the inversion of the synthetic FTG data, panels (a9) and (b9) of Figure 10 show better results than those for the inversion of gravity field only.

In the next numerical experiment, we have considered a more complicated model of the background density. In this setting, we would typically expect the encasing sediment densities to increase with depth (roughly following the seismic velocity trends); we might also

1  
2  
3  
4  
5  
6  
7  
8  
9  
10  
11  
12  
13  
14  
15  
16  
17  
18  
19  
20  
21  
22  
23  
24  
25  
26  
27  
28  
29  
30  
31  
32  
33  
34  
35  
36  
37  
38  
39  
40  
41  
42  
43  
44  
45  
46  
47  
48  
49  
50  
51  
52  
53  
54  
55  
56  
57  
58  
59  
60

expect the shallow top salt to be a positive density contrast with respect to the sediments, the middle portion (tabular salt) to be nearly the same density as the sediments, and the deeper portion of the salt body to be less dense than the sediments. In order to model this situation, we have assumed that the density of the background varies from  $0 \text{ g/cm}^3$  (top) to  $0.2 \text{ g/cm}^3$  (bottom). All the synthetic data were contaminated by 1% Gaussian noise. The 1% is the peak noise level of the synthetic observed data, where the mean value and the standard deviation are 0.5% and 0.17%, respectively. Figure 11 shows the synthetic gravity field of the SEG salt model with the background density varied with depth. The two white lines in this figure indicate the location of profiles A ( $Y = 1900 \text{ m}$ ) and B ( $Y = 2600 \text{ m}$ ). For the gravity data inversion, the vertical cross sections of the synthetic model are given in Figure 12, panels (a2) and (b2), while panels (a3)-(b3) and (a4)-(b4) show the cross sections of the recovered models produced by the conventional smooth (minimum norm) and multinary inversions, respectively. Figure 13 shows the inversion results of the synthetic FTG data at profiles A and B. One can see that for a more complex model with variable background density, it is difficult to determine the shape of the salt body correctly using gravity field  $G_z$ . In this case, the FTG data inversion provides a stronger density anomaly, but the shape of the body was not determined correctly. The results of this study demonstrate the practical limitation of the proposed gravity inversion.

Next, we will apply the multinary inversion to the FTG data collected at the Nordkapp Basin.

## CASE STUDY: MULTINARY INVERSION OF FTG DATA AT THE NORDKAPP BASIN

The Nordkapp basin is a deep narrow salt basin in the southern Barents Sea (Figure 14, modified from Worsley (2008)). The south-western part of the Nordkapp Basin (Obelix survey location, in Figure 15) is a narrow, north east-trending sub-basin 150 km long and 25-50 km wide. It contains some 17 salt diapirs located along the basin’s axis (Figure 15, modified from Gernigon et al (2011)). The north eastern part is a wider east-trending sub-basin about 200 km long and 50-70 km wide. More than 16 salt diapirs occur west of the 32° E meridian. Exploration in the Nordkapp basin started in the 1980’s but remained limited until the early 1990’s (Nielsen et al., 1995; Henriksen and Vorren, 1996). Recent improvements in the interpretation of the basin’s structural history and discovery of hydrocarbons in wells outside the basin suggest it as a promising exploration target (Bugge et al., 2002).

Figures 14 depicts the main structural elements in the Barents sea and the Nordkapp Basin with FTG survey location. The predominant exploration features known from this area are the complex salt diapirs (see Figure 15) and their related structural traps. The marine FTG survey was acquired by Bell Geospace on behalf of StatoilHydro (Dr. Farrelly, personal communication).

Much of the present uncertainty and exploration risk associated with these salt features results from severe seismic imaging/distortion problems and subsequent interpretation ambiguity of the salt isopach (specifically the ability to seismically define/map the salt base). Figure 16 presents an example of depth migrated profile (line L1 in Figure 17 ) from 3D survey showing salt feature F2 and typical imaging ambiguity of high resolution seismic.

1  
2  
3  
4  
5  
6  
7  
8  
9  
10  
11  
12  
13  
14  
15  
16  
17  
18  
19  
20  
21  
22  
23  
24  
25  
26  
27  
28  
29  
30  
31  
32  
33  
34  
35  
36  
37  
38  
39  
40  
41  
42  
43  
44  
45  
46  
47  
48  
49  
50  
51  
52  
53  
54  
55  
56  
57  
58  
59  
60

One should expect that FTG data can provide additional information for evaluation of these complex salt geometries. It can be used to define geological boundaries with strong density contrasts, typical for salt dome structures.

In order to improve the imaging quality of the salt structures, a 3D multinary inversion has been applied to the FTG data. Note that, the bathymetry was not taken into account in this inversion, because it is relatively flat in the area of the survey. The maps of the  $G_{zz}$  component of the FTG data are given in Figure 17, where the major targets of the study area were the salt diapirs, G2 and F2. We ran the multinary inversion for the  $G_{zz}$ ,  $G_{zx}$  and  $G_{zy}$  FTG components. We have selected a modeling domain 28 km (east-west)  $\times$  17 km (north-south) and extended at a depth of 6 km. The volume of inversion was discretized into  $281 \times 171 \times 60$  cells, where the cell size was  $100 \text{ m} \times 100 \text{ m} \times 100 \text{ m}$ . A typical density of the host rocks in the target area is within  $2.30\text{-}2.38 \text{ g/cm}^3$ . Salt diapirs are usually characterized by the negative density anomalies. Thus, the multinary function was set to recover three discrete densities of  $0 \text{ g/cm}^3$ ,  $-0.4 \text{ g/cm}^3$  and  $0.2 \text{ g/cm}^3$  (where value 0 represented the background density model). These values were chosen based on the results of the previous study by Wan and Zhdanov (2013). In this inversion of case study, the adaptive standard deviation  $\sigma$  was applied with the initial value  $\sigma_1 = 0.05$  and the upper limit  $\sigma_{\max} = 0.08$ . The increment of standard deviation ( $\delta\sigma$ ) was selected as 0.001. Figures 18 and 19 show the approximate representation of the multinary model transform (panel a) and its derivative, Gaussian function (panel b), when  $\sigma = 0.05$  and 0.08, respectively. The inversion was run until the norm of difference between the predicted and observed data reached 7.5%. Figure 20, panel (a) presents a misfit plot for this inversion, which reached the level of 7.48% at iteration number 248. Convergence plots of both the misfit and parametric functionals illustrate a stable convergence of the multinary inversion for this

target area. Panel (b) shows the variation of standard deviation,  $\sigma$ , during the adaptive multinary inversion.

Figures 21 through 23 show the maps of the observed FTG data versus the predicted data for  $G_{zz}$ ,  $G_{zx}$  and  $G_{zy}$  components, respectively. Figure 24 (a~c) shows a comparison between the observed FTG data (red line) used for multinary inversion and the predicted data (blue line) for the FTG components along the A-A' profile. One can see a very good data fitting. The panels (d) and (e) show the cross sections of the recovered models using the conventional smooth and multinary inversions along the A-A' profile, respectively. One can see that, the conventional inversion can only show a weak anomaly for the salt diapir, G2; however the multinary inversion recovers the boundaries of the salt body with sharp density contrast very well. This can be also shown by the inversion result along the B-B' profile in Figure 25. Figure 26 shows the horizontal cross sections at a depth of 3000 m for the recovered models. Note that, these results are in good correlation with the images obtained by iterative migration of the FTG data (Wan and Zhdanov, 2013); however, the multinary inversion produces a sharper density contrast.

Figure 16 (b) shows a combination plot of the seismic profile L1 with the recovered density distribution using the multinary approach in the same location. One can note that the flanks and the salt base are clearly seen in this figure; however, the density structure of the salt diapir appears to be slightly more compact than in the seismic image. Thus, the inversion results demonstrate that the multinary inversion approach has a strong potential to improve the quality of the conventional gravity inversion for geological targets with sharp density contrast, e.g., a salt dome structure.

1  
2  
3  
4  
5  
6  
7  
8  
9  
10  
11  
12  
13  
14  
15  
16  
17  
18  
19  
20  
21  
22  
23  
24  
25  
26  
27  
28  
29  
30  
31  
32  
33  
34  
35  
36  
37  
38  
39  
40  
41  
42  
43  
44  
45  
46  
47  
48  
49  
50  
51  
52  
53  
54  
55  
56  
57  
58  
59  
60

CONCLUSION

We have developed an adaptive multinary inversion method to solve the gravity and gravity gradiometry inverse problem with the anomalous bodies characterized by a finite number of discrete values of the densities. We have demonstrated that this inverse problem can be solved using gradient-type optimization method with adaptive selection of the standard deviation of the corresponding multinary transform. We have tested this method with two 3D synthetic models: a two-body model and a modified SEG salt dome density model. The results of our modeling studies demonstrated that multinary inversion can recover the approximate shapes and locations of the anomalous bodies well at their true densities. We have also applied this method to the FTG data of the Nordkapp Basin and located the salt diapirs with sharp density contrast. Thus, the results of our studies demonstrate that the novel adaptive multinary inversion approach has a strong potential to improve the quality of the conventional smooth gravity inversion for geological targets with sharp density contrast, e.g., a salt dome structure.

ACKNOWLEDGEMENTS

The authors acknowledge support from the University of Utah’s Consortium for Electromagnetic Modeling and Inversion (CEMI) and TechnoImaging. We thank Dr. Cox for his valuable suggestions.

We are thankful to Dr. Brian Farrelly for providing the FTG data.

The authors also thank the reviewers, Dr. Ed Biegert and Dr. Julio Lyrio, for their useful suggestions which helped to improve the manuscript.

1  
2  
3  
4  
5  
6  
7  
8  
9  
10  
11  
12  
13  
14  
15  
16  
17  
18  
19  
20  
21  
22  
23  
24  
25  
26  
27  
28  
29  
30  
31  
32  
33  
34  
35  
36  
37  
38  
39  
40  
41  
42  
43  
44  
45  
46  
47  
48  
49  
50  
51  
52  
53  
54  
55  
56  
57  
58  
59  
60

## REFERENCES

1  
2  
3  
4  
5  
6  
7  
8  
9  
10  
11  
12  
13  
14  
15  
16  
17  
18  
19  
20  
21  
22  
23  
24  
25  
26  
27  
28  
29  
30  
31  
32  
33  
34  
35  
36  
37  
38  
39  
40  
41  
42  
43  
44  
45  
46  
47  
48  
49  
50  
51  
52  
53  
54  
55  
56  
57  
58  
59  
60

Bosch, M., A. Guillen and P. Ledru, 2001, Lithologic tomography: an application to geophysical data from the Cadomian belt of northern Brittany, France: *Tectonophysics*, **331**, 197-227.

Bugge, T., G. Elvebakk, S. Fanavoll, G. Mangerud, M. Smelror, H. M. Weiss, and K. Nilsen, 2002, Shallow stratigraphic drilling applied in hydrocarbon exploration of the Nordkapp Basin, Barents Sea: *Marine and Petroleum Geology*, **19** (1), 13-37.

Constable, S. C., R. L. Parker, and C. G. Constable, 1987, Occam's inversion: A practical algorithm for generating smooth models from electromagnetic sounding data: *Geophysics*, **52**, 289-300.

Dorn, O., and D. Lesselier, 2006, Level set methods for inverse scattering: *Inverse Problems*, **22**, R67-R131.

Gernigon, L., Brønner, M., Fichler, C., Løvås, L., Marellø, L. and Olesen, O., 2011, Magnetic expression of salt diapir-related structures in the Nordkapp Basin, western Barents Sea. *Geology*, **39**(2), 135-138.

Henriksen, S. and T. O. Vorren, 1996, Early Tertiary sedimentation and salt tectonics in the Nordkapp Basin; southern Barents Sea: *Norsk Geologisk Tidsskrift*, **76** 33-44.

Krahenbuhl, R. A., and Y. Li, 2006, Inversion of gravity data using a binary formulation: *Geophysical Journal International*, **167**, 543-556.

Lelièvre, P.G., Farquharson, C.G. and Hurich, C.A., 2012. Joint inversion of seismic traveltimes and gravity data on unstructured grids with application to mineral exploration. *Geophysics*, **77** (1), K1-K15.

1  
2  
3  
4  
5  
6  
7  
8  
9  
10  
11  
12  
13  
14  
15  
16  
17  
18  
19  
20  
21  
22  
23  
24  
25  
26  
27  
28  
29  
30  
31  
32  
33  
34  
35  
36  
37  
38  
39  
40  
41  
42  
43  
44  
45  
46  
47  
48  
49  
50  
51  
52  
53  
54  
55  
56  
57  
58  
59  
60

Li, W., W. Lu, and J. Qian 2016, A level-set method for imaging salt structures using gravity data: *Geophysics*, **81** (2), G27-G40.

Neilsen, K. T., B. C. Vendeville, and J. T. Johansen, 1995, Influence of regional tectonics on halokinesis in the Norkapp Basin, Barents Sea; in M.P. Jackson, D. G. Roberts, and S. Snelson, Eds., *Salt Tectonics: a global perspective: AAPG Memoir* **65**, 413-436.

Osher, S., and J.A. Sethian, 1988, Fronts propagating with curvature-dependent speed: algorithms based on Hamilton-Jacobi formulations: *Journal of Computational Physics*, **79**, 12-49.

Paasche, H., Tronicke, J., Holliger, K., Green, A.G. and Maurer, H., 2006, Integration of diverse physical-property models: Subsurface zonation and petrophysical parameter estimation based on fuzzy c-means cluster analyses. *Geophysics*, **71** (3), H33-H44.

Portniaguine, O., and M. S. Zhdanov, 1999, Focusing geophysical inversion images: *Geophysics*, **64**, 874-887.

Santosa, F., 1996, A level set approach for inverse problems involving obstacles: *ESAIM: Control, Optimisation and Calculus of Variations* **1**, 17-33.

Sun, J. and Li, Y., 2015. Multidomain petrophysically constrained inversion and geology differentiation using guided fuzzy c-means clustering. *Geophysics*, **80** (4), ID1-ID18.

Tikhonov, A. N., and V. Y. Arsenin, 1977, *Solutions of ill-posed problems*: V. H. Winston and Sons, New York.

Wan, L., and M. S. Zhdanov, 2013, Iterative migration of gravity and gravity gradiometry data: *Proceedings of the Annual Meeting of the Consortium for Electromagnetic Modeling and Inversion*, The University of Utah, 3-34.

1  
2  
3  
4 Worsley, D., 2008, The post-Caledonian development of Svalbard and the western Bar-  
5 ents Sea. *Polar Research*, **27** (3), 298-317.  
6  
7

8 Zhdanov, M. S., 2002, *Geophysical inverse theory and regularization problems*: Elsevier.  
9

10 Zhdanov, M. S., 2009, New advances in regularized inversion of gravity and electromag-  
11 netic data: *Geophysical Prospecting*, **57**, 463-478.  
12  
13

14 Zhdanov, M. S., 2015, *Inverse theory and applications in geophysics*, Elsevier.  
15

16 Zhdanov, M. S., and L. Cox, 2013, Multinary inversion of geophysical data: Proceedings  
17 of the Annual Meeting of the Consortium for Electromagnetic Modeling and Inversion, The  
18 University of Utah, 125-136.  
19  
20  
21  
22  
23  
24  
25  
26  
27  
28  
29  
30  
31  
32  
33  
34  
35  
36  
37  
38  
39  
40  
41  
42  
43  
44  
45  
46  
47  
48  
49  
50  
51  
52  
53  
54  
55  
56  
57  
58  
59  
60

## LIST OF FIGURES

1 Model 1. An example of the multinary function of the third order: (a) a *cumulative density probability function*, (b) its derivative (*probability density function*). The values of the discrete densities are as follows:  $-1.0 \text{ g/cm}^3$ ,  $0.0 \text{ g/cm}^3$ ,  $0.5 \text{ g/cm}^3$ , and  $\sigma = 0.02$ .

2 Model 1. Panel (a): Predicted gravity field (solid line) vs. synthetic gravity field  $G_z$  (dotted line) along the profile at  $Y = 3500 \text{ m}$  (Northing). Panel (b): vertical cross section of the synthetic model. Panels (c), (d) and (e) provide the same cross sections of the recovered density distribution using the conventional, focusing, and multinary inversions, respectively.

3 Model 1. 3D views of the synthetic model (panel a) and the inversion result (panel b). The cut off values of the densities are  $> 0.45 \text{ g/cm}^3$  for a large body and  $< -0.9 \text{ g/cm}^3$  for a small body.).

4 Model 1. Panel (a) shows the approximate representations of the multinary model transform, and panel (b) shows its derivative, Gaussian function, with the wrong densities (dotted line) and the right densities (solid line). The values of the wrong and right discrete densities are  $[-0.7, 0.0, 0.35]$  and  $[-1.0, 0.0, 0.5]$ , respectively, and  $\sigma = 0.02$ .

5 Model 1. Panels (a) and (b): Predicted gravity field (solid line) vs. synthetic observed gravity field  $G_z$  (dotted line) along the profile at  $Y = 3500 \text{ m}$  (Northing) computed using the multinary inversion with the right densities and the wrong densities, respectively. Panels (c) and (d) provide the same cross sections of the recovered density distribution as Fig.1 using the multinary inversion with the right densities and the wrong densities, respectively.

6 A 3D view of the SEG salt model.

7 Model 2. Panel (a) shows the approximate representation of the multinary model

1  
2  
3  
4  
5  
6  
7  
8  
9  
10  
11  
12  
13  
14  
15  
16  
17  
18  
19  
20  
21  
22  
23  
24  
25  
26  
27  
28  
29  
30  
31  
32  
33  
34  
35  
36  
37  
38  
39  
40  
41  
42  
43  
44  
45  
46  
47  
48  
49  
50  
51  
52  
53  
54  
55  
56  
57  
58  
59  
60

transform, and panel (b) shows its derivative, Gaussian function. The values of the discrete densities are as follows:  $-0.5 \text{ g/cm}^3$  and  $0.0 \text{ g/cm}^3$ , and  $\sigma = 0.05$ .

8 Model 2-1. Gravity field of the SEG salt model. The white lines show profiles A and B.

9 Model 2-1: Predicted gravity field (solid lines) vs. synthetic gravity data (dotted lines) along the profile A at  $Y = 1900 \text{ m}$  (Northing) for (a1)  $G_z$  component. Panel (a2) presents the vertical cross section of the synthetic model. Panels (a3) and (a4) provide the same cross sections of the recovered density distribution produced by conventional inversion and multinary inversion, respectively. Panels (b1)~(b4) show the same figures for profile B at  $Y = 2600 \text{ m}$  (Northing).

10 Model 2-1: Predicted FTG field (solid line) vs. synthetic FTG data (dotted line) along profile A at  $Y = 1900 \text{ m}$  (Northing) for (a1)  $G_{zz}$ , (a2)  $G_{zx}$ , (a3)  $G_{zy}$ , (a4)  $G_{xx}$ , (a5)  $G_{yy}$  and (a6)  $G_{xy}$  components. Panel (a7) presents the vertical cross section of the synthetic model. Panels (a8) and (a9) provide the same cross sections of the recovered density distribution obtained by conventional inversion and multinary inversion, respectively. Panels (b1)~(b9) show the same figures for profile B at  $Y = 2600 \text{ m}$  (Northing).

11 Model 2-2. Gravity field of the SEG salt model with variable background. The white lines show profiles A and B.

12 Model 2-2: Predicted gravity field (solid line) vs. synthetic gravity data (dotted line) along profile A at  $Y = 1900 \text{ m}$  (Northing) for (a1)  $G_z$  component. Panel (a2) presents the vertical cross section of the synthetic model. Panels (a3) and (a4) provide the same cross sections of the recovered density distribution using conventional inversion and multinary inversion, respectively. Panels (b1)~(b4) show the same figures for profile B at  $Y = 2600 \text{ m}$  (Northing).

1  
2  
3  
4  
5  
6  
7  
8  
9  
10  
11  
12  
13  
14  
15  
16  
17  
18  
19  
20  
21  
22  
23  
24  
25  
26  
27  
28  
29  
30  
31  
32  
33  
34  
35  
36  
37  
38  
39  
40  
41  
42  
43  
44  
45  
46  
47  
48  
49  
50  
51  
52  
53  
54  
55  
56  
57  
58  
59  
60

1  
2  
3  
4  
5  
6  
7  
8  
9  
10  
11  
12  
13  
14  
15  
16  
17  
18  
19  
20  
21  
22  
23  
24  
25  
26  
27  
28  
29  
30  
31  
32  
33  
34  
35  
36  
37  
38  
39  
40  
41  
42  
43  
44  
45  
46  
47  
48  
49  
50  
51  
52  
53  
54  
55  
56  
57  
58  
59  
60

13 Model 2-2: Predicted FTG field (solid line) vs. synthetic FTG data (dotted line) along the profile A at  $Y = 1900$  m (Northing) for (a1)  $G_{zz}$ , (a2)  $G_{zx}$ , (a3)  $G_{zy}$ , (a4)  $G_{xx}$ , (a5)  $G_{yy}$  and (a6)  $G_{xy}$  components. Panel (a7) presents the vertical cross section of the synthetic model. Panels (a8) and (a9) provide the same cross sections of the recovered density distribution using conventional inversion and multinary inversion, respectively. Panels (b1)~(b9) show the same figures for the profile B at  $Y = 2600$  m (Northing).

14 Main structural elements in the Barents Sea area, location of Nordkapp Basin and 3D FTG survey. Modified from Worsley (2008).

15 Simplified structural map of the Nordkapp Basin showing salt diapirs and main fault zones. Modified from Gernigon et al (2011).

16 Panel (a) presents a depth migrated profile (line L1 in Figure ??) from 3D seismic survey showing salt feature F2. Panel (b) shows the same seismic profile (L1) overlapped with the cross section of the result of multinary gravity in the same location.

17 Case study. Map of the  $G_{zz}$  component of the FTG data with the salt diapirs F2 and G2. The white lines show the location of the A-A' and B-B' profiles and the seismic survey line L1.

18 Case study. Panel (a) shows the approximate representation of the multinary model transform, and panel (b) shows its derivative, Gaussian function. The values of the discrete densities are as follows:  $-0.4 \text{ g/cm}^3$ ,  $0.0 \text{ g/cm}^3$ ,  $0.2 \text{ g/cm}^3$ , and  $\sigma = 0.05$ .

19 Case study. Panel (a) shows the approximate representation of the multinary model transform, and panel (b) shows its derivative, Gaussian function. The values of the discrete densities are as follows:  $-0.4 \text{ g/cm}^3$ ,  $0.0 \text{ g/cm}^3$ ,  $0.2 \text{ g/cm}^3$ , and  $\sigma = 0.08$ .

20 Case study. Panel (a) presents the convergence plots of the misfit (dashed line) and parametric functional (solid line) vs. the iteration number. Panel (b) shows the variation

of the standard deviation  $\sigma$  during the adaptive multinary inversion.

21 Case study. Maps of the observed FTG data (panel a) and the predicted gravity field  $G_{zz}$  (panel b), and their differences (panel c).

22 Case study. Maps of the observed FTG data (panel a) and the predicted gravity field  $G_{zx}$  (panel b), and their differences (panel c).

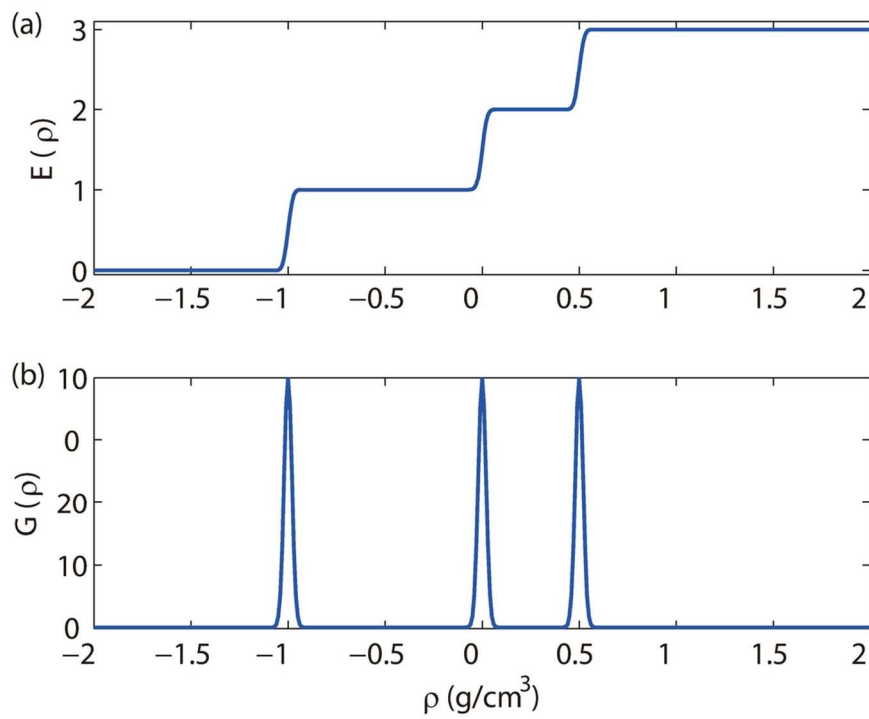
23 Case study. Maps of the observed FTG data (panel a) and the predicted gravity field  $G_{zy}$  (panel b), and their differences (panel c).

24 Case study. Predicted gravity field (blue line) vs. observed FTG data (red line) along the A-A' profile for (a)  $G_{zz}$ , (b)  $G_{zx}$  and (c)  $G_{zy}$  components. Panels (d) and (e) provide the cross sections of the recovered density distribution using conventional inversion and multinary inversion, respectively.

25 Case study. Predicted gravity field (blue line) vs. observed FTG data (red line) along the B-B' profile for (a)  $G_{zz}$ , (b)  $G_{zx}$  and (c)  $G_{zy}$  components. Panels (d) and (e) provide the cross sections of the recovered density distribution using conventional inversion and multinary inversion, respectively.

26 Case study. Horizontal section of the recovered model at a depth of 3000 m.

1  
2  
3  
4  
5  
6  
7  
8  
9  
10  
11  
12  
13  
14  
15  
16  
17  
18  
19  
20  
21  
22  
23  
24  
25  
26  
27  
28  
29  
30  
31  
32  
33  
34  
35  
36  
37  
38  
39  
40  
41  
42  
43  
44  
45  
46  
47  
48  
49  
50  
51  
52  
53  
54  
55  
56  
57  
58  
59  
60

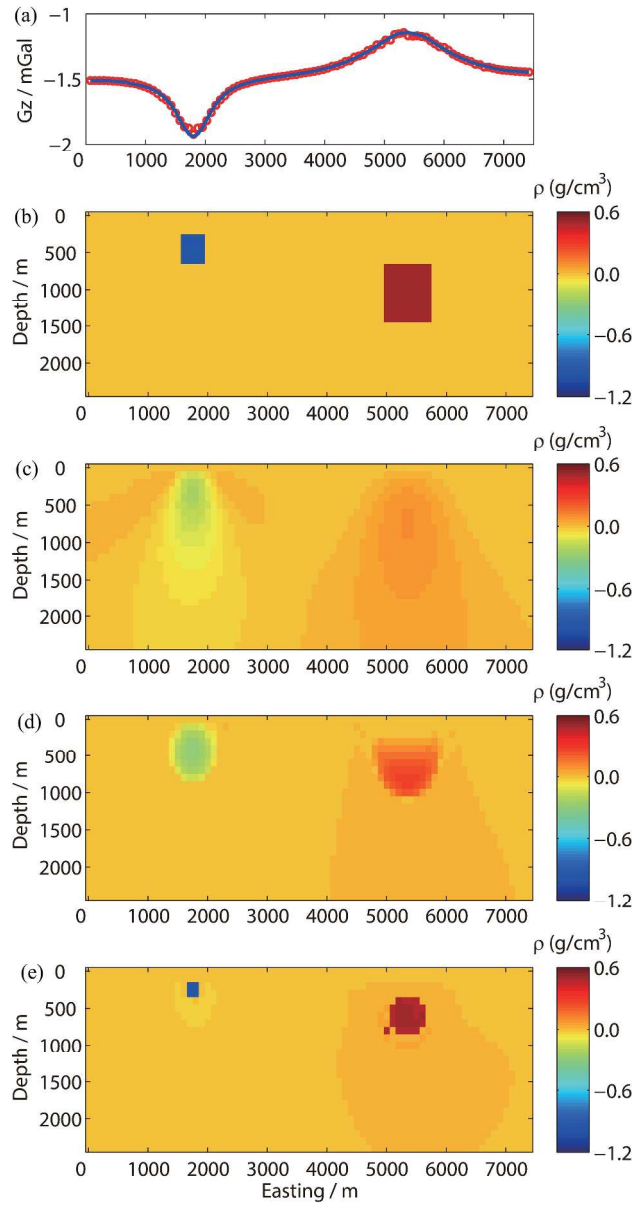


1

111x83mm (300 x 300 DPI)

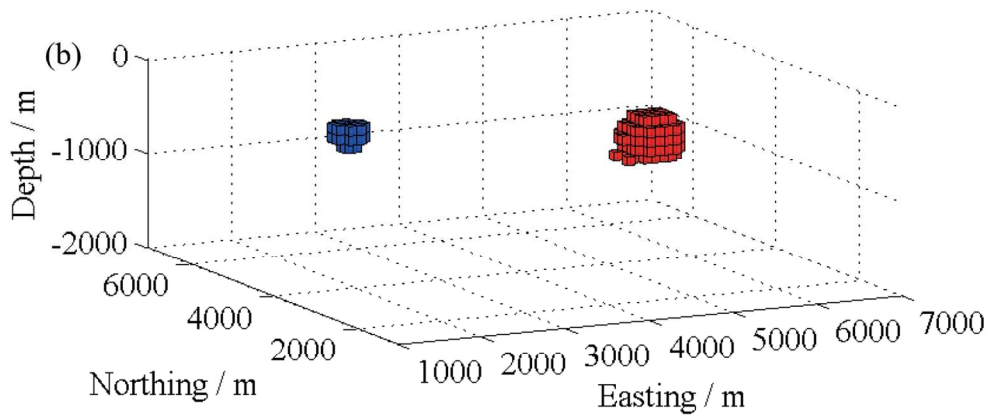
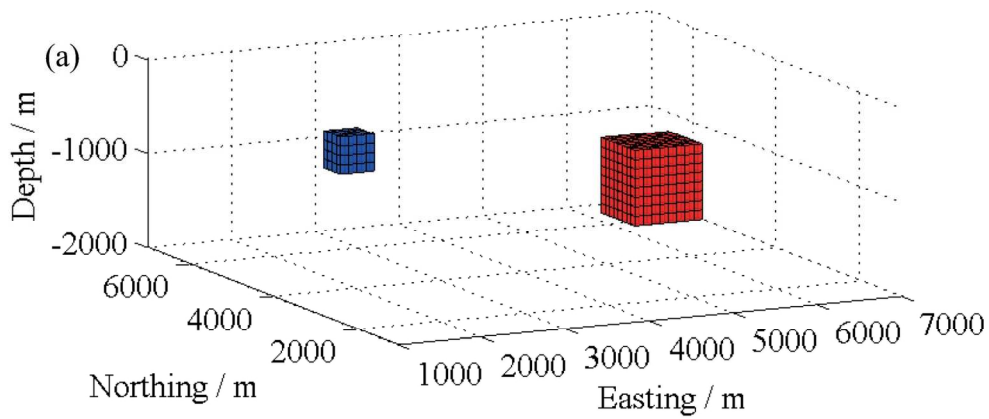
1  
2  
3  
4  
5  
6  
7  
8  
9  
10  
11  
12  
13  
14  
15  
16  
17  
18  
19  
20  
21  
22  
23  
24  
25  
26  
27  
28  
29  
30  
31  
32  
33  
34  
35  
36  
37  
38  
39  
40  
41  
42  
43  
44  
45  
46  
47  
48  
49  
50  
51  
52  
53  
54  
55  
56  
57  
58  
59  
60

1  
2  
3  
4  
5  
6  
7  
8  
9  
10  
11  
12  
13  
14  
15  
16  
17  
18  
19  
20  
21  
22  
23  
24  
25  
26  
27  
28  
29  
30  
31  
32  
33  
34  
35  
36  
37  
38  
39  
40  
41  
42  
43  
44  
45  
46  
47  
48  
49  
50  
51  
52  
53  
54  
55  
56  
57  
58  
59  
60



2

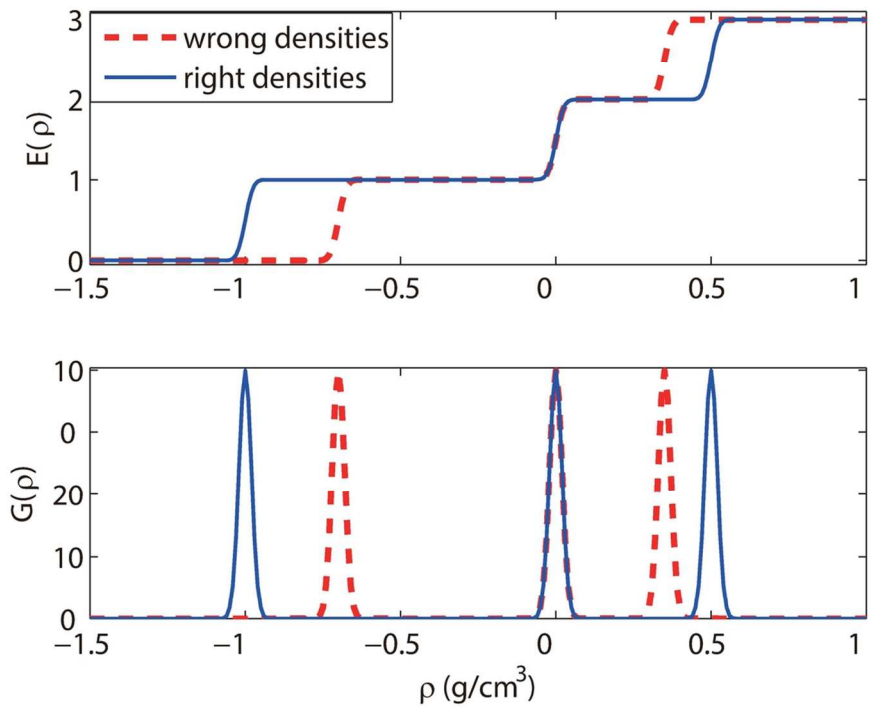
262x460mm (300 x 300 DPI)



3

140x137mm (300 x 300 DPI)

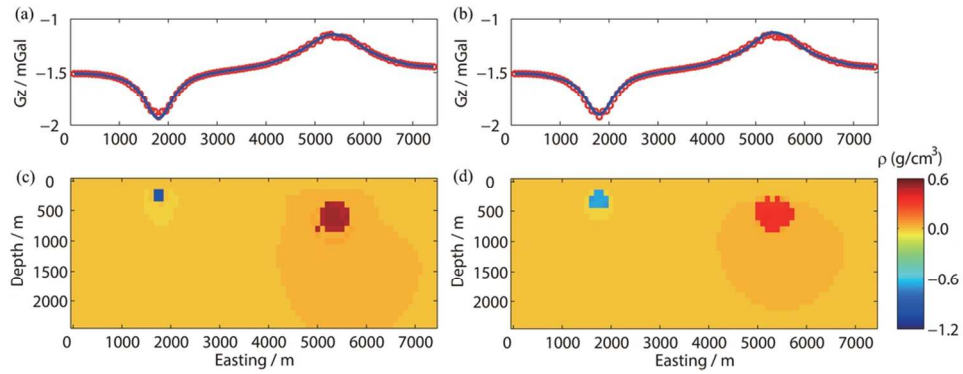
1  
2  
3  
4  
5  
6  
7  
8  
9  
10  
11  
12  
13  
14  
15  
16  
17  
18  
19  
20  
21  
22  
23  
24  
25  
26  
27  
28  
29  
30  
31  
32  
33  
34  
35  
36  
37  
38  
39  
40  
41  
42  
43  
44  
45  
46  
47  
48  
49  
50  
51  
52  
53  
54  
55  
56  
57  
58  
59  
60



4

111x83mm (300 x 300 DPI)

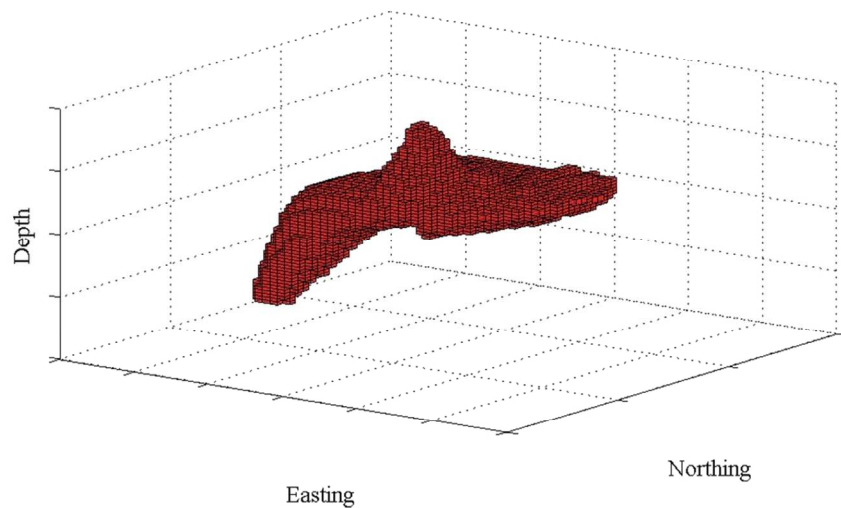
1  
2  
3  
4  
5  
6  
7  
8  
9  
10  
11  
12  
13  
14  
15  
16  
17  
18  
19  
20  
21  
22  
23  
24  
25  
26  
27  
28  
29  
30  
31  
32  
33  
34  
35  
36  
37  
38  
39  
40  
41  
42  
43  
44  
45  
46  
47  
48  
49  
50  
51  
52  
53  
54  
55  
56  
57  
58  
59  
60



5

97x35mm (300 x 300 DPI)

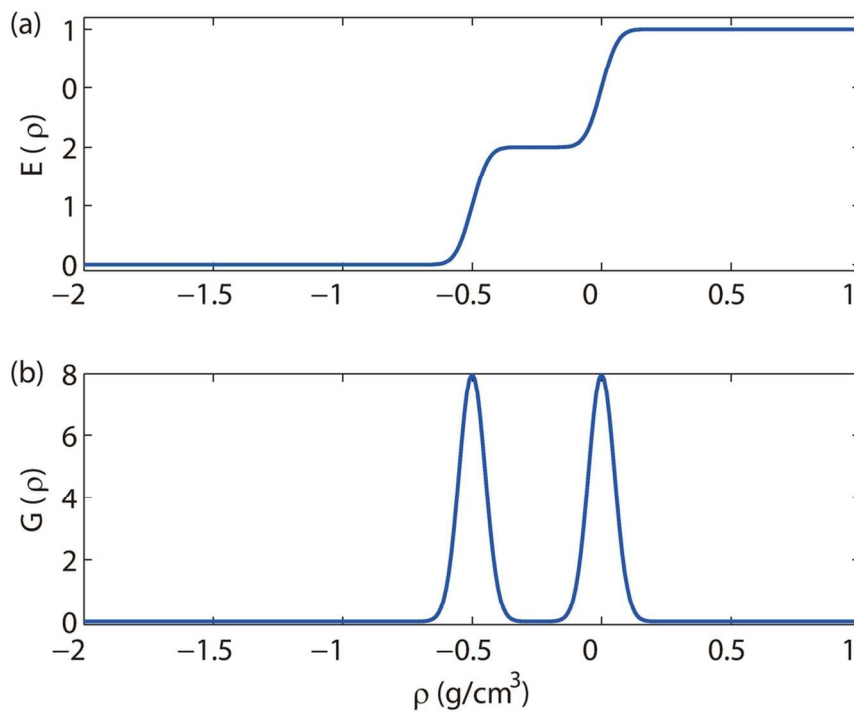
1  
2  
3  
4  
5  
6  
7  
8  
9  
10  
11  
12  
13  
14  
15  
16  
17  
18  
19  
20  
21  
22  
23  
24  
25  
26  
27  
28  
29  
30  
31  
32  
33  
34  
35  
36  
37  
38  
39  
40  
41  
42  
43  
44  
45  
46  
47  
48  
49  
50  
51  
52  
53  
54  
55  
56  
57  
58  
59  
60



6

101x54mm (300 x 300 DPI)

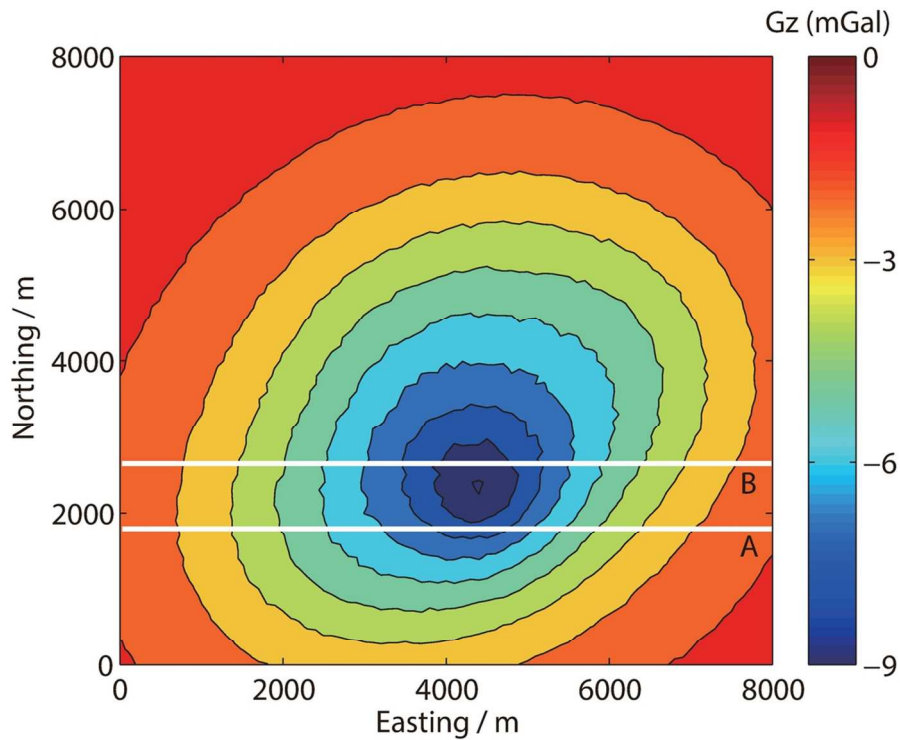
1  
2  
3  
4  
5  
6  
7  
8  
9  
10  
11  
12  
13  
14  
15  
16  
17  
18  
19  
20  
21  
22  
23  
24  
25  
26  
27  
28  
29  
30  
31  
32  
33  
34  
35  
36  
37  
38  
39  
40  
41  
42  
43  
44  
45  
46  
47  
48  
49  
50  
51  
52  
53  
54  
55  
56  
57  
58  
59  
60



7

111x83mm (300 x 300 DPI)

1  
2  
3  
4  
5  
6  
7  
8  
9  
10  
11  
12  
13  
14  
15  
16  
17  
18  
19  
20  
21  
22  
23  
24  
25  
26  
27  
28  
29  
30  
31  
32  
33  
34  
35  
36  
37  
38  
39  
40  
41  
42  
43  
44  
45  
46  
47  
48  
49  
50  
51  
52  
53  
54  
55  
56  
57  
58  
59  
60

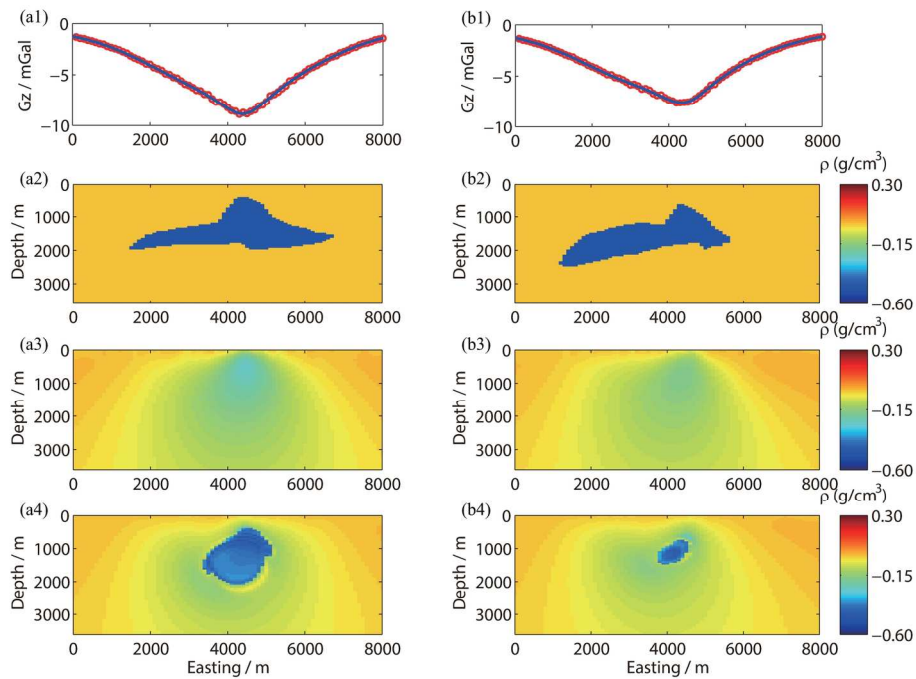


8

111x83mm (300 x 300 DPI)

1  
2  
3  
4  
5  
6  
7  
8  
9  
10  
11  
12  
13  
14  
15  
16  
17  
18  
19  
20  
21  
22  
23  
24  
25  
26  
27  
28  
29  
30  
31  
32  
33  
34  
35  
36  
37  
38  
39  
40  
41  
42  
43  
44  
45  
46  
47  
48  
49  
50  
51  
52  
53  
54  
55  
56  
57  
58  
59  
60

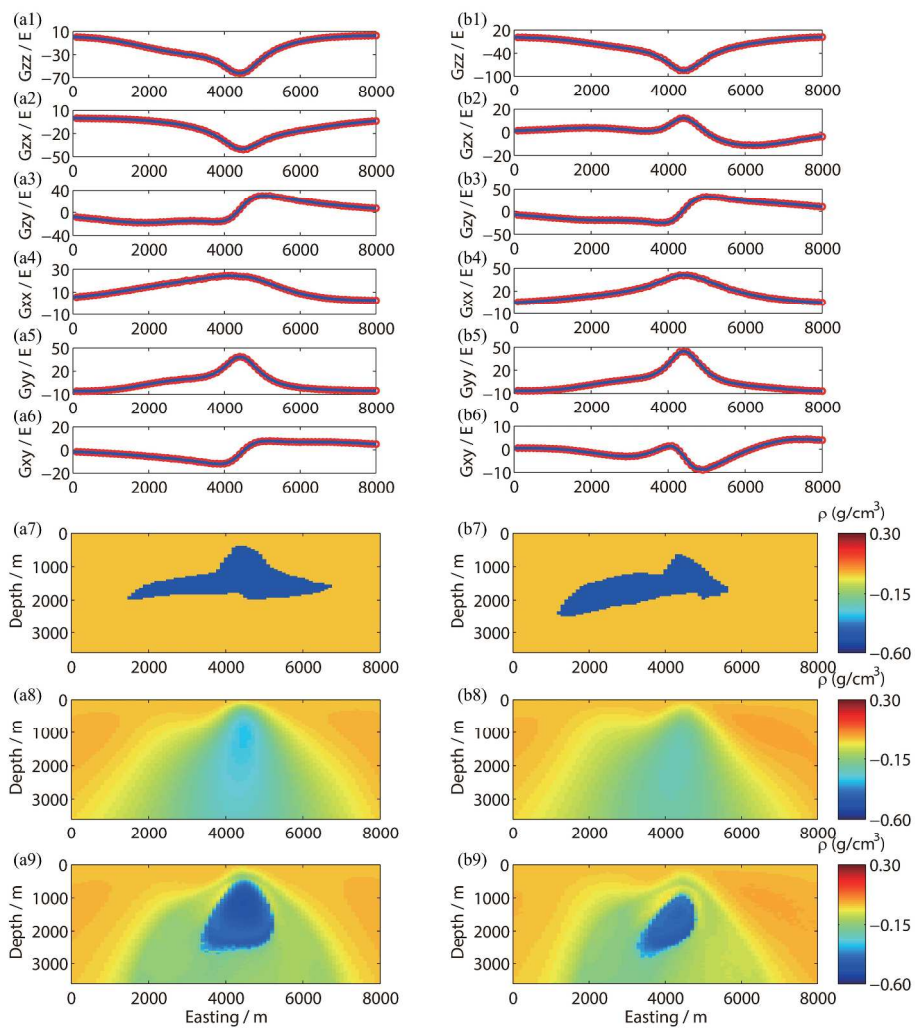
1  
2  
3  
4  
5  
6  
7  
8  
9  
10  
11  
12  
13  
14  
15  
16  
17  
18  
19  
20  
21  
22  
23  
24  
25  
26  
27  
28  
29  
30  
31  
32  
33  
34  
35  
36  
37  
38  
39  
40  
41  
42  
43  
44  
45  
46  
47  
48  
49  
50  
51  
52  
53  
54  
55  
56  
57  
58  
59  
60



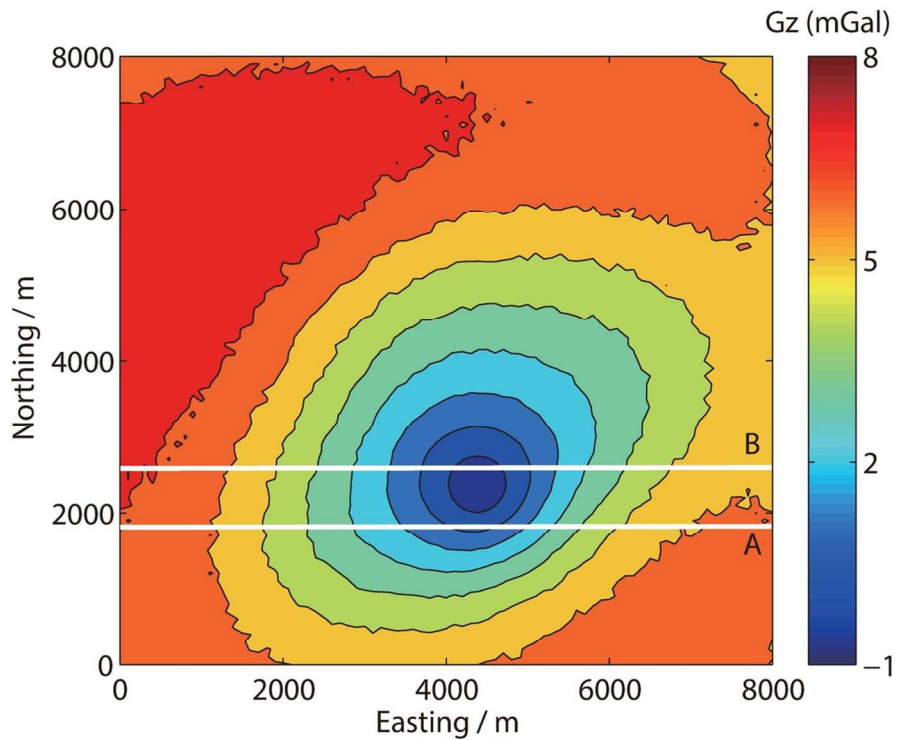
9

177x122mm (300 x 300 DPI)

1  
2  
3  
4  
5  
6  
7  
8  
9  
10  
11  
12  
13  
14  
15  
16  
17  
18  
19  
20  
21  
22  
23  
24  
25  
26  
27  
28  
29  
30  
31  
32  
33  
34  
35  
36  
37  
38  
39  
40  
41  
42  
43  
44  
45  
46  
47  
48  
49  
50  
51  
52  
53  
54  
55  
56  
57  
58  
59  
60



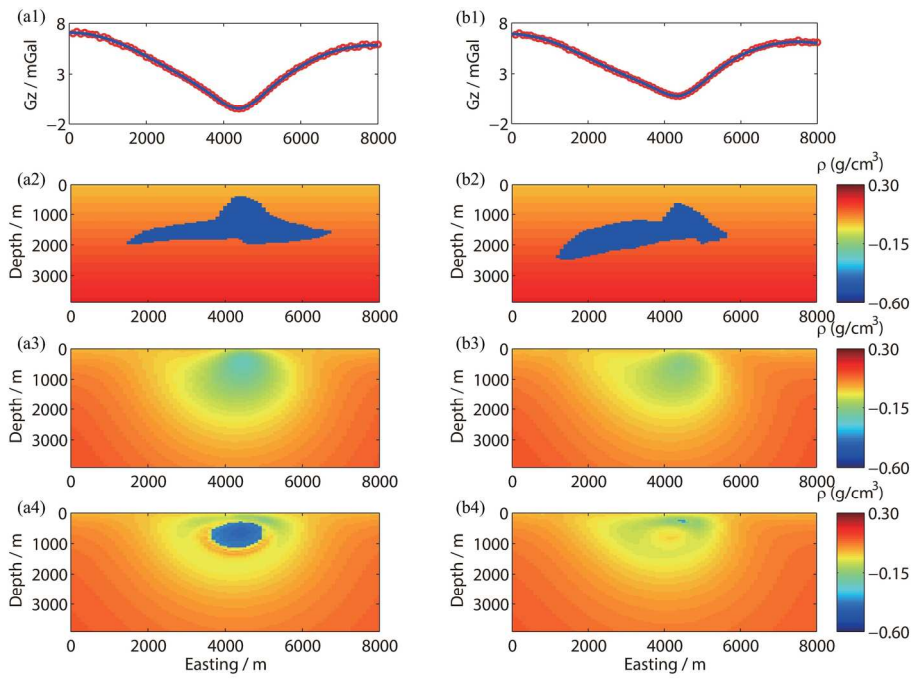
1  
2  
3  
4  
5  
6  
7  
8  
9  
10  
11  
12  
13  
14  
15  
16  
17  
18  
19  
20  
21  
22  
23  
24  
25  
26  
27  
28  
29  
30  
31  
32  
33  
34  
35  
36  
37  
38  
39  
40  
41  
42  
43  
44  
45  
46  
47  
48  
49  
50  
51  
52  
53  
54  
55  
56  
57  
58  
59  
60



11

111x83mm (300 x 300 DPI)

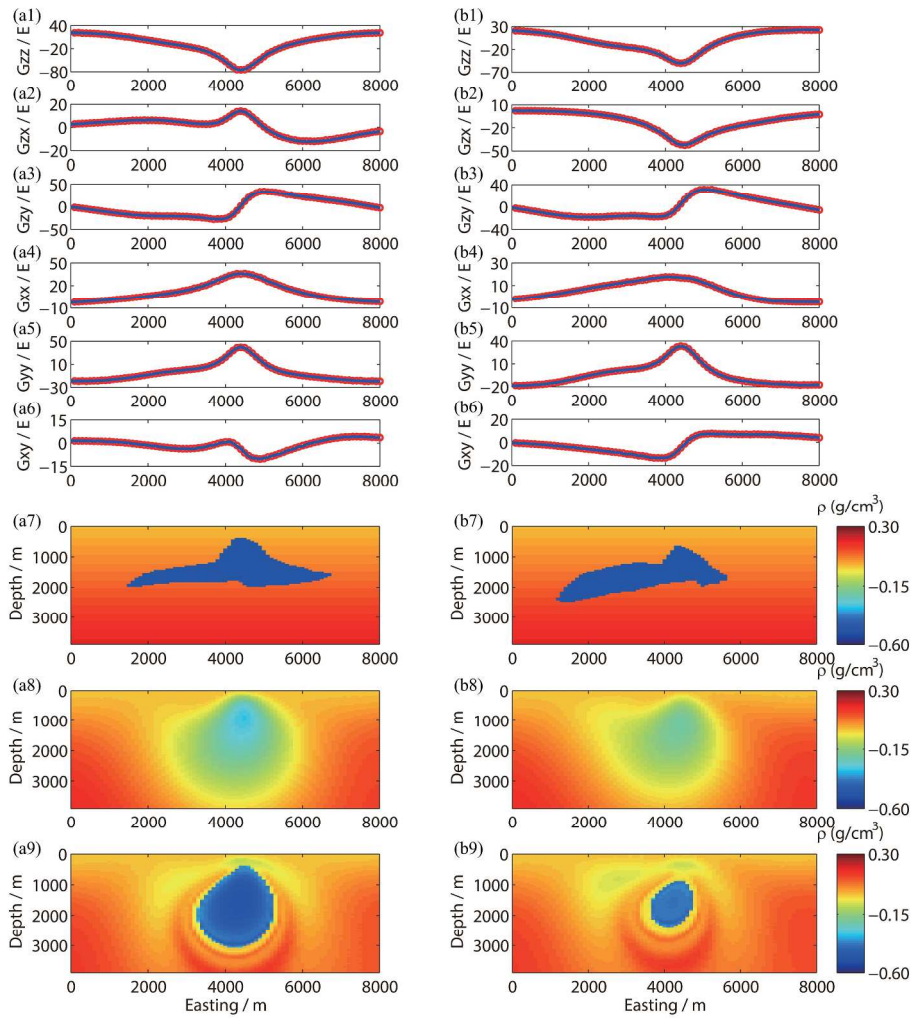
1  
2  
3  
4  
5  
6  
7  
8  
9  
10  
11  
12  
13  
14  
15  
16  
17  
18  
19  
20  
21  
22  
23  
24  
25  
26  
27  
28  
29  
30  
31  
32  
33  
34  
35  
36  
37  
38  
39  
40  
41  
42  
43  
44  
45  
46  
47  
48  
49  
50  
51  
52  
53  
54  
55  
56  
57  
58  
59  
60

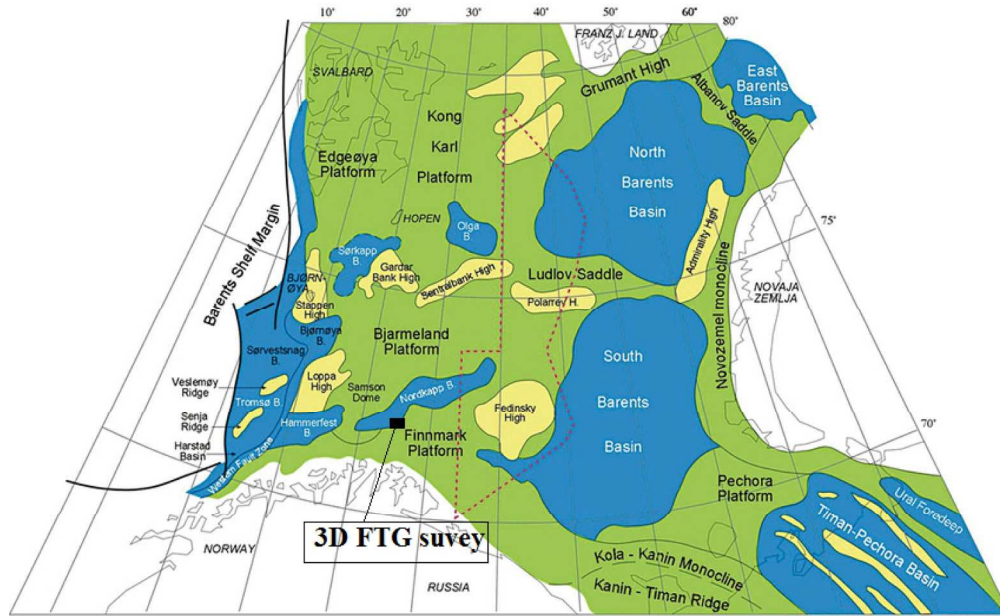


12

177x122mm (300 x 300 DPI)

1  
2  
3  
4  
5  
6  
7  
8  
9  
10  
11  
12  
13  
14  
15  
16  
17  
18  
19  
20  
21  
22  
23  
24  
25  
26  
27  
28  
29  
30  
31  
32  
33  
34  
35  
36  
37  
38  
39  
40  
41  
42  
43  
44  
45  
46  
47  
48  
49  
50  
51  
52  
53  
54  
55  
56  
57  
58  
59  
60

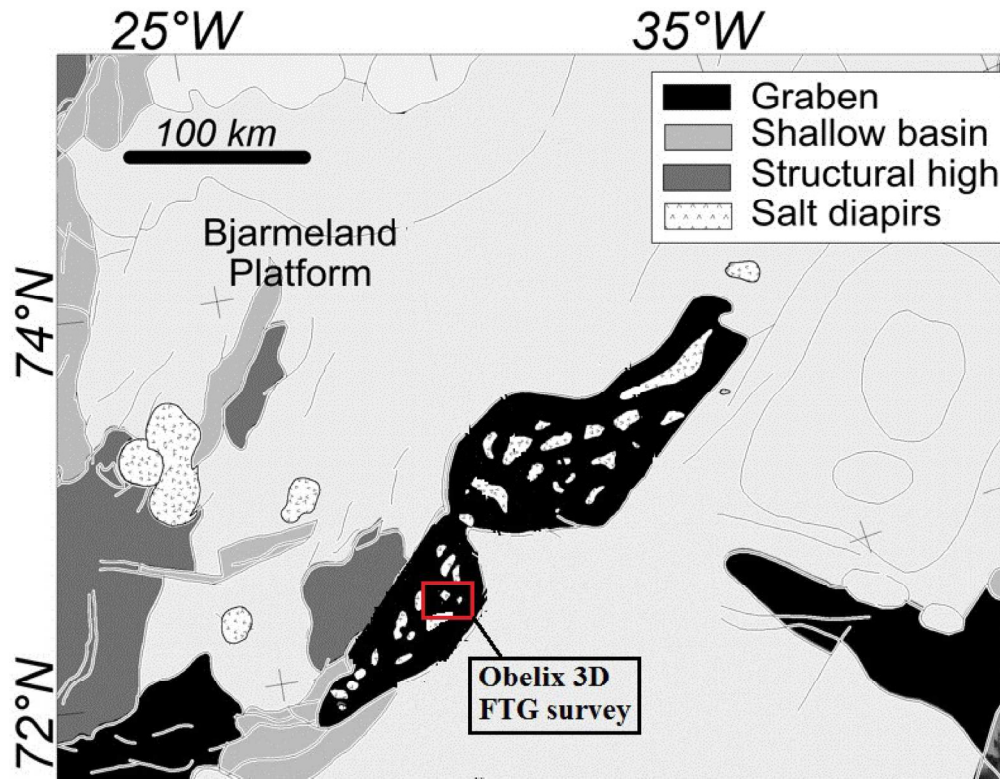




14

183x112mm (300 x 300 DPI)

1  
2  
3  
4  
5  
6  
7  
8  
9  
10  
11  
12  
13  
14  
15  
16  
17  
18  
19  
20  
21  
22  
23  
24  
25  
26  
27  
28  
29  
30  
31  
32  
33  
34  
35  
36  
37  
38  
39  
40  
41  
42  
43  
44  
45  
46  
47  
48  
49  
50  
51  
52  
53  
54  
55  
56  
57  
58  
59  
60

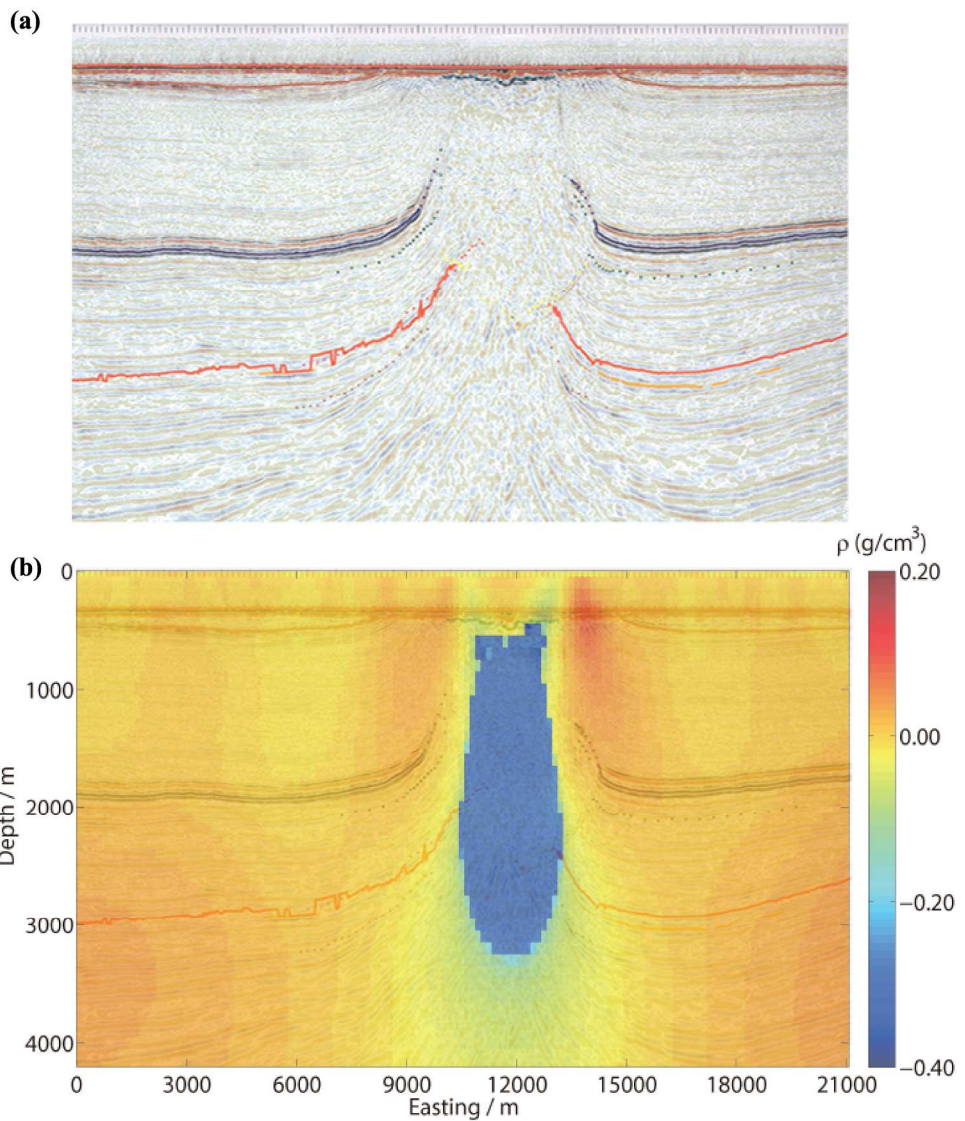


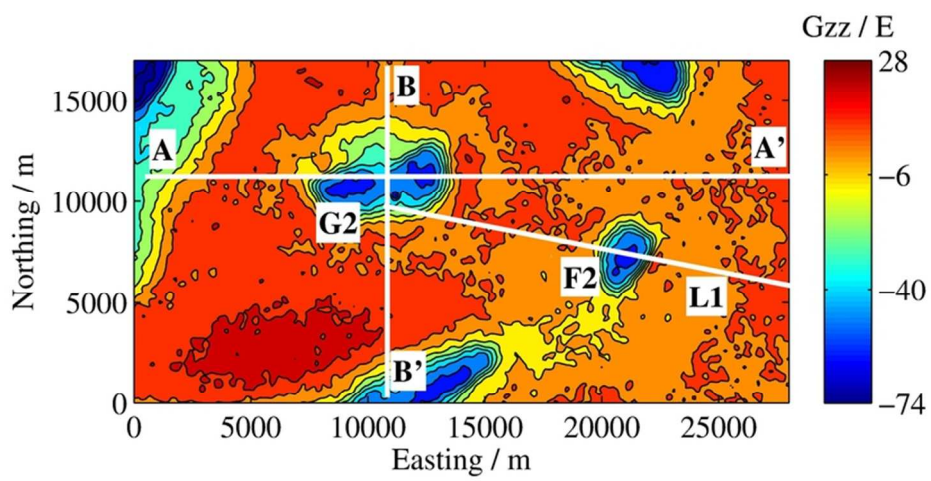
15

161x124mm (300 x 300 DPI)

1  
2  
3  
4  
5  
6  
7  
8  
9  
10  
11  
12  
13  
14  
15  
16  
17  
18  
19  
20  
21  
22  
23  
24  
25  
26  
27  
28  
29  
30  
31  
32  
33  
34  
35  
36  
37  
38  
39  
40  
41  
42  
43  
44  
45  
46  
47  
48  
49  
50  
51  
52  
53  
54  
55  
56  
57  
58  
59  
60

1  
2  
3  
4  
5  
6  
7  
8  
9  
10  
11  
12  
13  
14  
15  
16  
17  
18  
19  
20  
21  
22  
23  
24  
25  
26  
27  
28  
29  
30  
31  
32  
33  
34  
35  
36  
37  
38  
39  
40  
41  
42  
43  
44  
45  
46  
47  
48  
49  
50  
51  
52  
53  
54  
55  
56  
57  
58  
59  
60

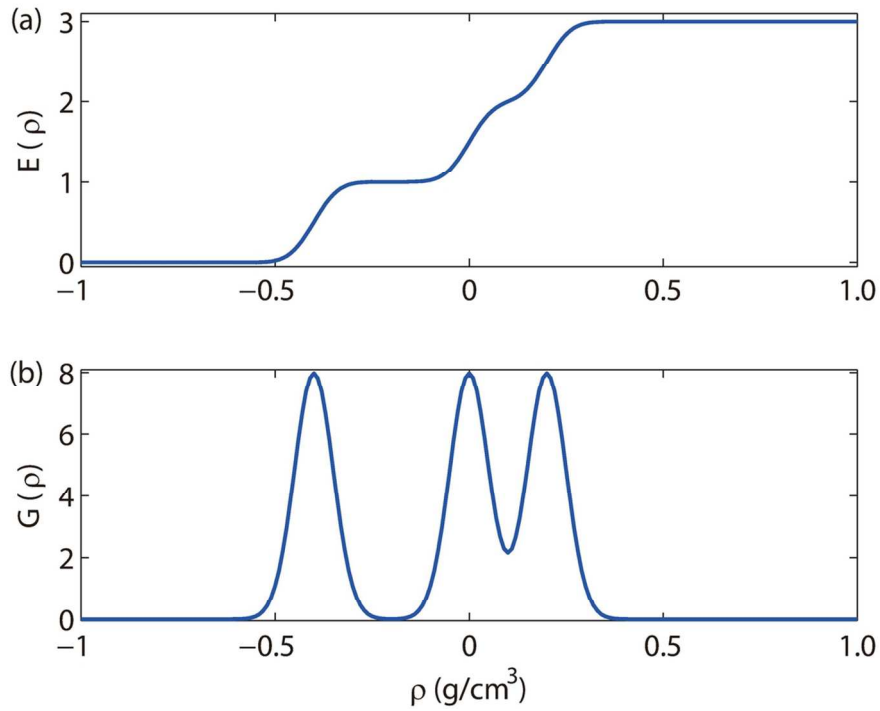




17

75x38mm (300 x 300 DPI)

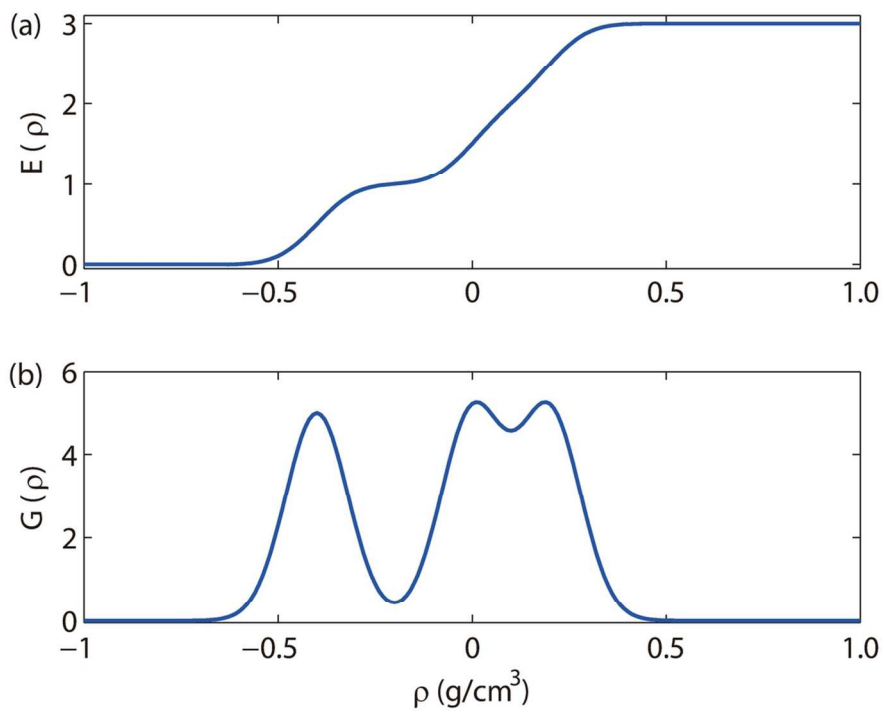
1  
2  
3  
4  
5  
6  
7  
8  
9  
10  
11  
12  
13  
14  
15  
16  
17  
18  
19  
20  
21  
22  
23  
24  
25  
26  
27  
28  
29  
30  
31  
32  
33  
34  
35  
36  
37  
38  
39  
40  
41  
42  
43  
44  
45  
46  
47  
48  
49  
50  
51  
52  
53  
54  
55  
56  
57  
58  
59  
60



18

111x83mm (300 x 300 DPI)

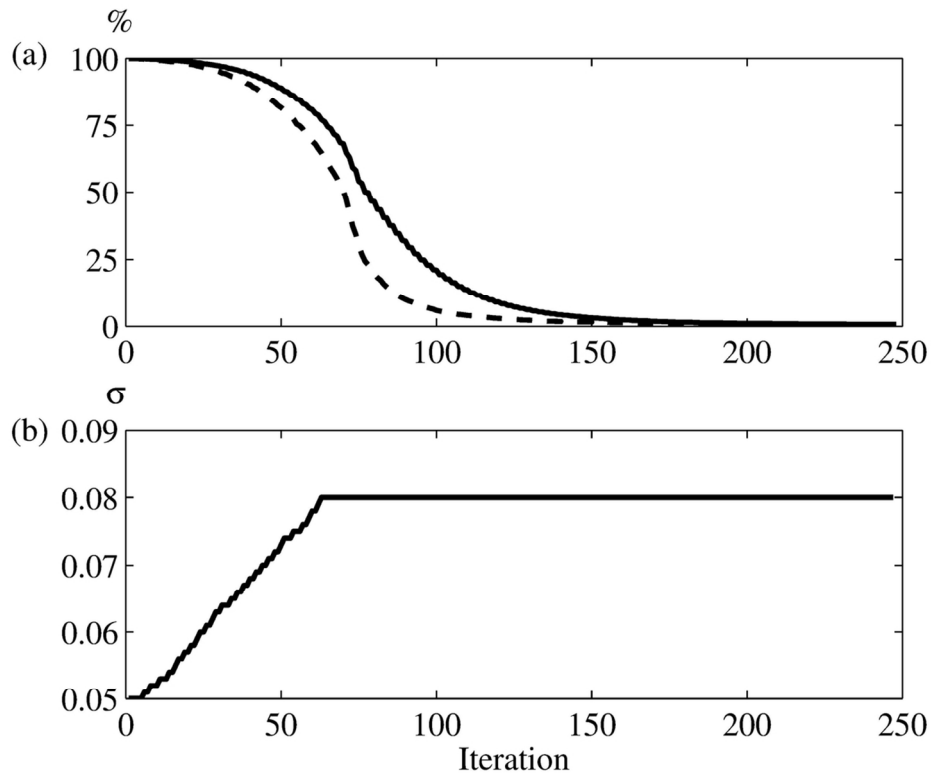
1  
2  
3  
4  
5  
6  
7  
8  
9  
10  
11  
12  
13  
14  
15  
16  
17  
18  
19  
20  
21  
22  
23  
24  
25  
26  
27  
28  
29  
30  
31  
32  
33  
34  
35  
36  
37  
38  
39  
40  
41  
42  
43  
44  
45  
46  
47  
48  
49  
50  
51  
52  
53  
54  
55  
56  
57  
58  
59  
60



19

111x83mm (300 x 300 DPI)

1  
2  
3  
4  
5  
6  
7  
8  
9  
10  
11  
12  
13  
14  
15  
16  
17  
18  
19  
20  
21  
22  
23  
24  
25  
26  
27  
28  
29  
30  
31  
32  
33  
34  
35  
36  
37  
38  
39  
40  
41  
42  
43  
44  
45  
46  
47  
48  
49  
50  
51  
52  
53  
54  
55  
56  
57  
58  
59  
60

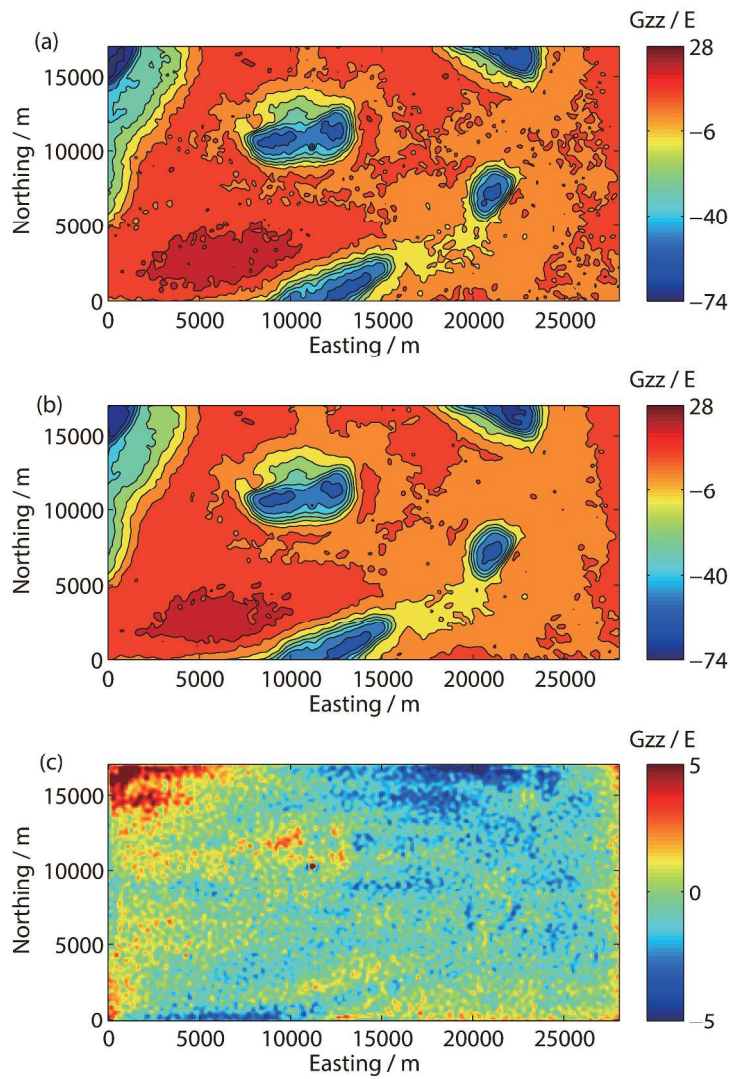


20

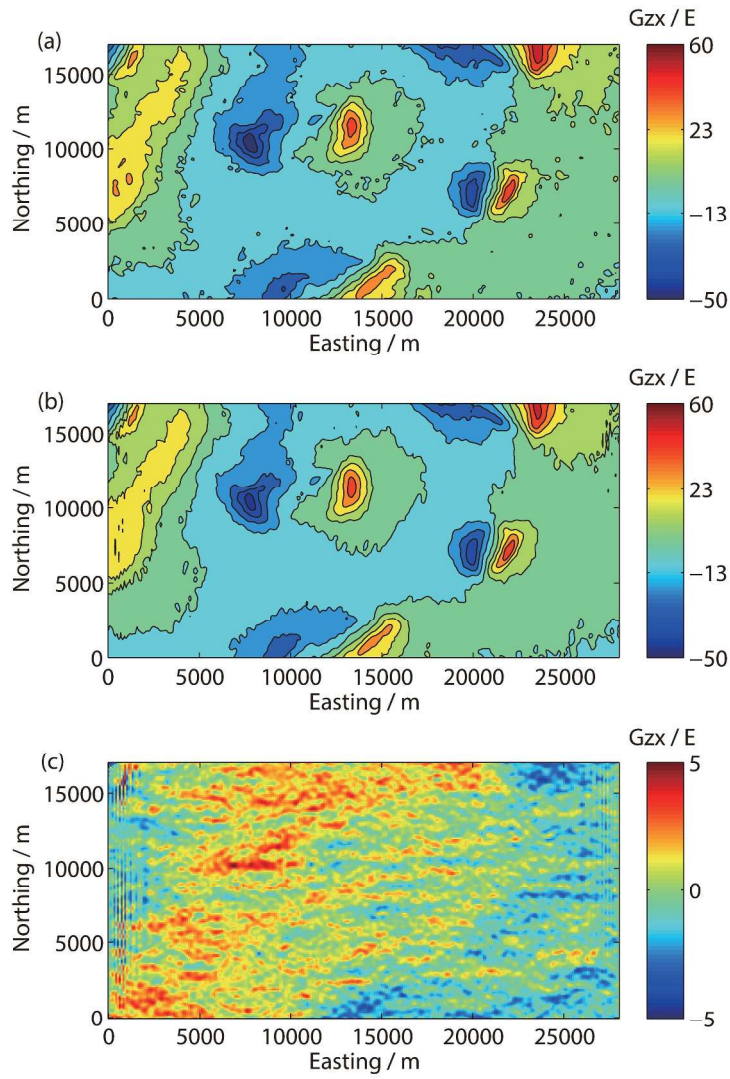
110x87mm (300 x 300 DPI)

1  
2  
3  
4  
5  
6  
7  
8  
9  
10  
11  
12  
13  
14  
15  
16  
17  
18  
19  
20  
21  
22  
23  
24  
25  
26  
27  
28  
29  
30  
31  
32  
33  
34  
35  
36  
37  
38  
39  
40  
41  
42  
43  
44  
45  
46  
47  
48  
49  
50  
51  
52  
53  
54  
55  
56  
57  
58  
59  
60

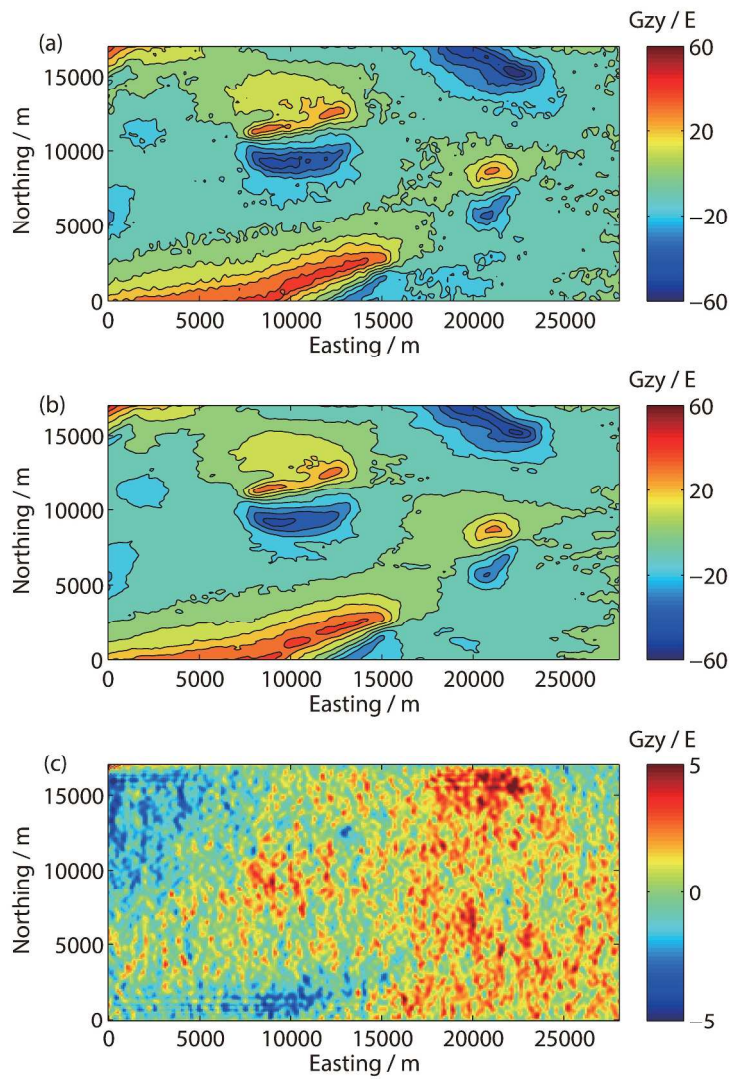
1  
2  
3  
4  
5  
6  
7  
8  
9  
10  
11  
12  
13  
14  
15  
16  
17  
18  
19  
20  
21  
22  
23  
24  
25  
26  
27  
28  
29  
30  
31  
32  
33  
34  
35  
36  
37  
38  
39  
40  
41  
42  
43  
44  
45  
46  
47  
48  
49  
50  
51  
52  
53  
54  
55  
56  
57  
58  
59  
60



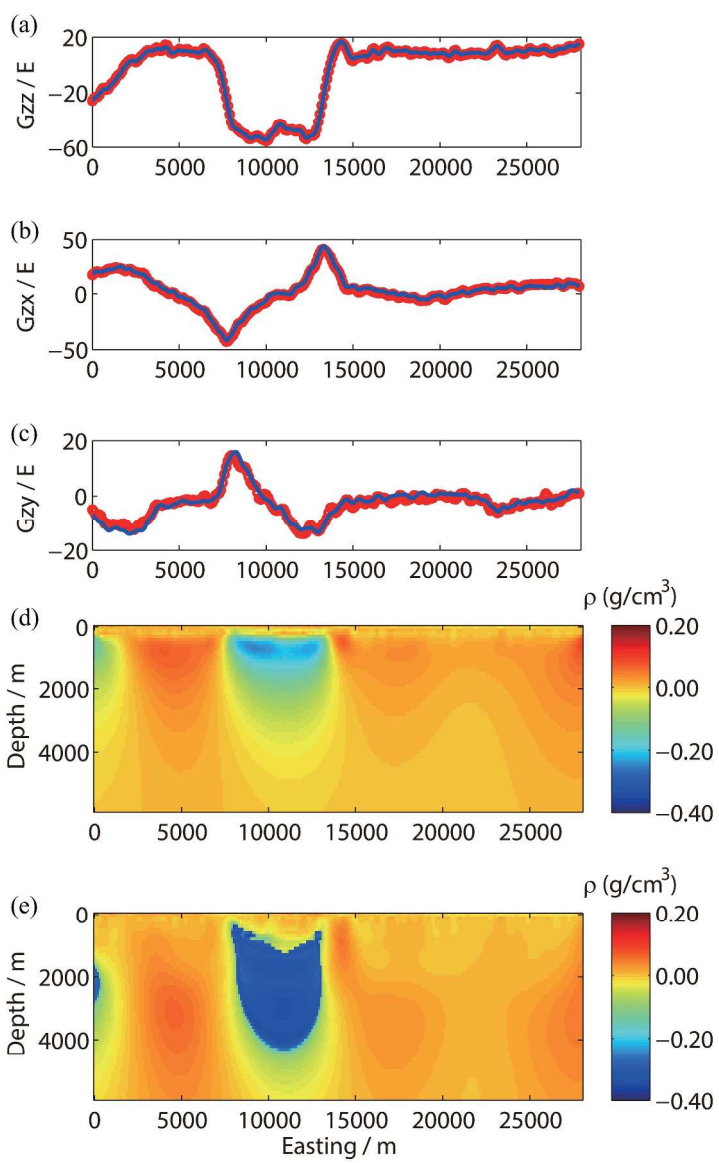
1  
2  
3  
4  
5  
6  
7  
8  
9  
10  
11  
12  
13  
14  
15  
16  
17  
18  
19  
20  
21  
22  
23  
24  
25  
26  
27  
28  
29  
30  
31  
32  
33  
34  
35  
36  
37  
38  
39  
40  
41  
42  
43  
44  
45  
46  
47  
48  
49  
50  
51  
52  
53  
54  
55  
56  
57  
58  
59  
60

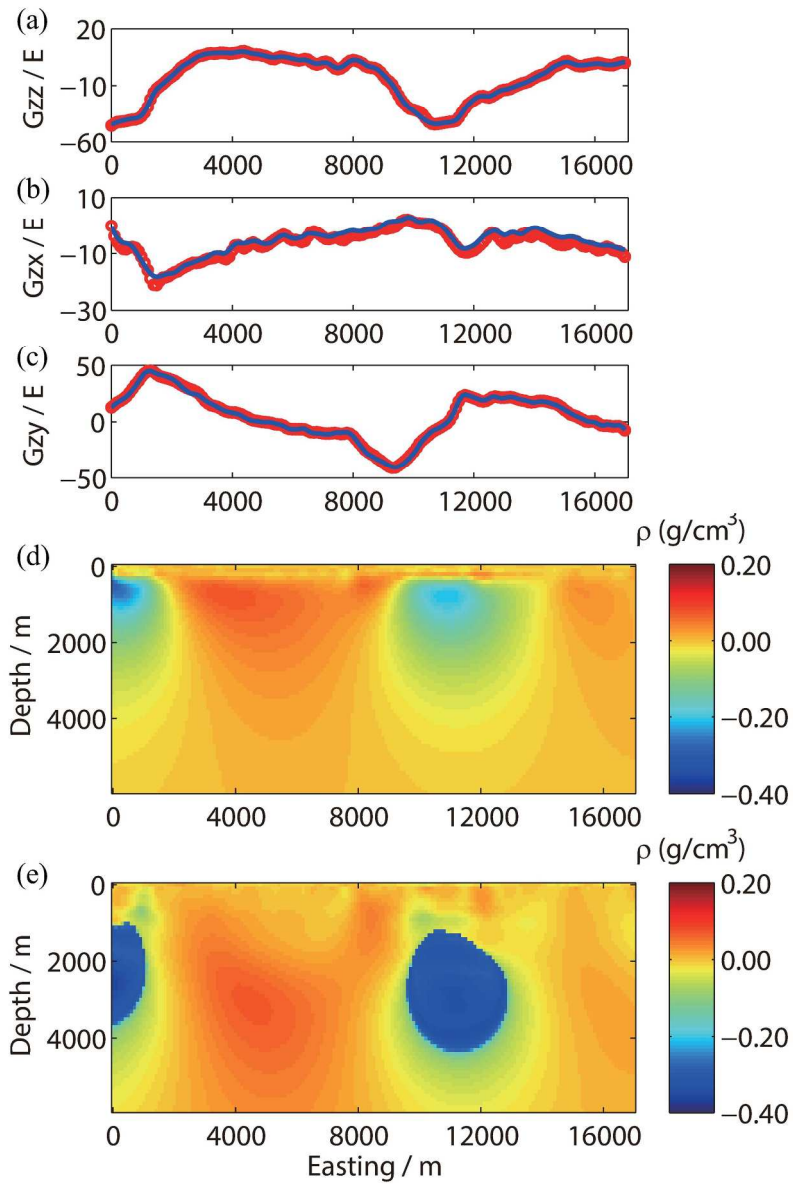


1  
2  
3  
4  
5  
6  
7  
8  
9  
10  
11  
12  
13  
14  
15  
16  
17  
18  
19  
20  
21  
22  
23  
24  
25  
26  
27  
28  
29  
30  
31  
32  
33  
34  
35  
36  
37  
38  
39  
40  
41  
42  
43  
44  
45  
46  
47  
48  
49  
50  
51  
52  
53  
54  
55  
56  
57  
58  
59  
60

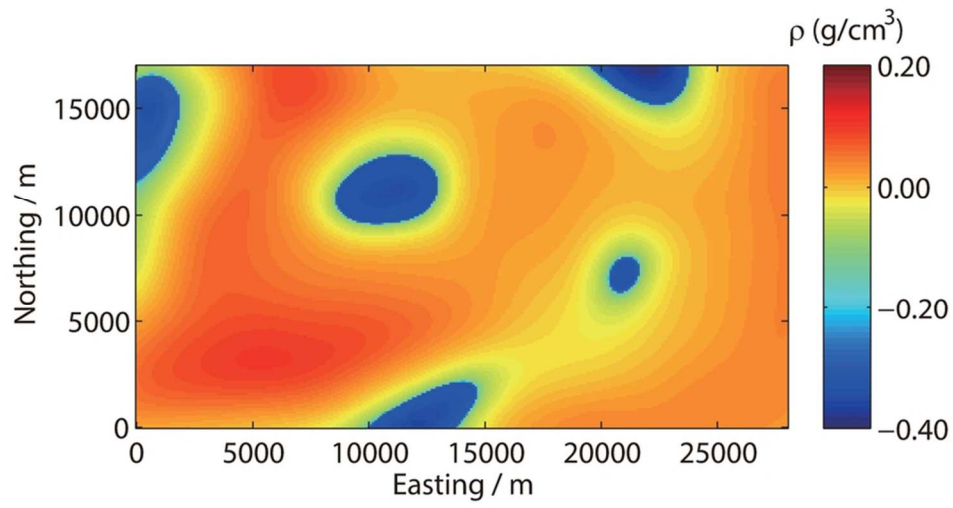


1  
2  
3  
4  
5  
6  
7  
8  
9  
10  
11  
12  
13  
14  
15  
16  
17  
18  
19  
20  
21  
22  
23  
24  
25  
26  
27  
28  
29  
30  
31  
32  
33  
34  
35  
36  
37  
38  
39  
40  
41  
42  
43  
44  
45  
46  
47  
48  
49  
50  
51  
52  
53  
54  
55  
56  
57  
58  
59  
60





1  
2  
3  
4  
5  
6  
7  
8  
9  
10  
11  
12  
13  
14  
15  
16  
17  
18  
19  
20  
21  
22  
23  
24  
25  
26  
27  
28  
29  
30  
31  
32  
33  
34  
35  
36  
37  
38  
39  
40  
41  
42  
43  
44  
45  
46  
47  
48  
49  
50  
51  
52  
53  
54  
55  
56  
57  
58  
59  
60



26

79x42mm (300 x 300 DPI)

1  
2  
3  
4  
5  
6  
7  
8  
9  
10  
11  
12  
13  
14  
15  
16  
17  
18  
19  
20  
21  
22  
23  
24  
25  
26  
27  
28  
29  
30  
31  
32  
33  
34  
35  
36  
37  
38  
39  
40  
41  
42  
43  
44  
45  
46  
47  
48  
49  
50  
51  
52  
53  
54  
55  
56  
57  
58  
59  
60